Applied Energy 307 (2022) 118159

Contents lists available at ScienceDirect

Applied Energy

journal homepage: www.elsevier.com/locate/apenergy

Nonlinear dynamics of a new energy harvesting system with quasi-zero stiffness

Jerzy Margielewicz [a], Damian Gąska [a,*], Grzegorz Litak [b], Piotr Wolszczak [b], Daniil Yurchenko [c]

[a] *Silesian University of Technology, Faculty of Transport and Aviation Engineering, Krasińskiego 8, Katowice 40-019, Poland*
[b] *Lublin University of Technology, Faculty of Mechanical Engineering, Nadbystrzycka 36, Lublin 20-618, Poland*
[c] *Institute of Mechanical, Process & Energy Engineering, Heriot-Watt University, Edinburgh EH14 4AS, UK*

HIGHLIGHTS

- A new energy harvesting system has been designed QZEH.
- The areas where the best energy harvesting is possible have been identified.
- The method of impulse excitation on the solution was proposed.
- The probability of the solution with the best effectivity was determined.

ARTICLE INFO

Keywords:
Lyapunov exponent
Basins of attraction
Diagram of solutions
Diagram of RMS voltage values
Diagram of impulse excitation
Nonlinear vibrations

ABSTRACT

This paper presents the results of modelling a new nonlinear multi-stable QZEH (quasi-zero energy harvester) system for harvesting energy from vibrating mechanical devices. Detailed tests were carried out on the system model, which consisted of a beam and a system of springs, which were used to determine the potential of a quasi-flat well. Two-dimensional distributions of the Lyapunov exponent were output from the numerical model, using the assumed range of variability within the control parameters, and plotted as a map in multi-color. These maps are related to diagrams of the RMS values of the voltage that is induced on the piezoelectric electrodes. To identify the optimal conditions for harvesting energy from mechanical vibrations, a multi-colored map of the RMS voltage values was produced. Its reference to the Lyapunov distribution map, showed that in the chaotic motion zones, energy harvesting is reduced. Based on the established sections of the Lyapunov exponent, diagrams of solutions (DS) showing the number of coexisting solutions and their periodicity were drawn. Multiple solutions and basins of attraction have been identified. On their basis it was possible to estimate the probability of obtaining a solution with the greatest energy harvesting efficiency. Moreover, a method of acting on the solution trajectory, by means of an impulse initiated at a specific moment in time, has been proposed. The results of the model tests were visualized as multi-colored maps of impulse excitations. The direct reference of the results of QZEH model tests to the tristable energy harvesting (TEH) system clearly indicates the advisability of using the QZEH system in terms of higher excitation amplitudes. The QZEH system also shows an improved ability to harvest energy in the low range of values of excitation frequencies.

1. Introduction

The subject of the research contained in this paper is a new system of harvesting energy from vibrating mechanical devices. From a technical point of view, it is possible to recover energy from the human environment in many ways. On an industrial scale, it is most often obtained from the so-called renewable energy sources, including solar energy, wind energy or water [1,2]. These sources are not always needed or available in large industrial sizes, and therefore an alternative approach is to use small and simple electromechanical systems that transform the energy of mechanical vibrations into electricity [3]. From a technical point of view, this is done via transducers: piezoelectric [4,5], electrostatic [6], or electromagnetic [7]. In fact, such solutions are characterized by relatively low energy efficiency, however, they are widely

---

* Corresponding author at: Silesian University of Technology, Faculty of Transport and Aviation Engineering, Krasińskiego 8, Katowice 40-019, Poland.
E-mail address: damian.gaska@polsl.pl (D. Gąska).

https://doi.org/10.1016/j.apenergy.2021.118159
Received 21 July 2021; Received in revised form 16 October 2021; Accepted 30 October 2021

available, and they are capable of powering simple electronic devices, such as sensors that are used to monitor the technical condition of devices and wireless data transmission systems.

Much research has been devoted to the issue of harvesting energy from vibrating mechanical devices [8], concerning, inter alia: identification of amplitude-frequency characteristics [9–11], experimental and model research of linear and non-linear transducer design solutions [12,13]. When carrying out numerical experiments, researchers usually adopt an equivalent electrical circuit that represents the electrical properties of the piezoelectric device. Such a circuit is most often mapped by a series connection of a capacitor and resistor. In the case of systems based on electromagnetic converters, their substitute electric circuit consists of a coil in series, connected with a resistor. It is also worth mentioning that, unlike piezoelectric transducers, the resistance of the equivalent circuit in electromagnetic transducers is negligible. For this reason, it is often overlooked during modelling. Bearing in mind the simplification of experimental and numerical tests, energy harvesting systems are most often loaded with a resistor that is connected to the converter [14,15].

From an engineering point of view, most design solutions are based on a flexible beam with piezoelectric transducers glued to it. Because, during the operation of machines, a wide spectrum of harmonic components are excited, solutions based on linear systems require many subsystems connected in parallel [16]. Each of which, is tuned to a different frequency [17]. The need to tune linear transducers to the appropriate harmonic components means that researchers focus their attention on nonlinear systems. Because in such systems it is possible to excite harmonics in a wide range of frequencies. Like linear systems, design solutions of nonlinear systems are based on flexible beams and contain additional elements in the form of permanent magnets [18]. These magnets are used to properly shape the energy potential in which the mechanical resonator moves. The mathematical description of the potential is most often mapped via polynomial functions [15,19,20]. Other design solutions are also known [21], consisting of two flexible beams, coupled by electric circuits [5] and mechanical systems [4,22,23]. There are also systems based on free and coupled single pendulums, or double pendulums [24].

Energy harvesting systems with local potential barriers are characterized by certain limitations, which are mainly caused by the required specific energy level of the external dynamic excitation [18,25]. The vibration level of the external source should be large enough to overcome the local potential barriers, because then the trajectories recorded on the phase plane reach the greatest possible displacement amplitudes. According to the authors, these limitations may be devoid of design solutions in which the energy potential is characterized by a flat, or almost flat, energy well. Such a potential barrier is characterized by a system with quasi-zero stiffness, the original purpose of which was vibration isolation in the range of low vibration frequencies [26]. Such systems have not been of wide interest so far in the context of harvesting energy from mechanical vibrations. A significant feature of the QZEH system being the subject of the research is the possibility of modifying the mechanical properties to adjust it to the conditions in which the energy is to be harvested.

The identification of steady-state periodic solutions becomes important because in nonlinear systems there may be many coexisting solutions differing in the efficiency of energy harvesting [27,28]. From the theoretical point of view, the most energy-efficient solutions are periodic solutions, characterized by a large amplitude of vibrations [18,29]. Methods for controlling dynamical systems [30,31], chaos control [32,33] are known. Nevertheless, from an energy harvesting point of view, this approach may be ineffective because the amount of energy supplied to the control system may be much greater than that harvested from vibration. With this in mind, an alternative method of influencing the nature of the solution is proposed. The change of the orbit of the solution can be achieved by initiating, in a strictly defined moment of time, an external impulse with a defined characteristic. Such excitation can, for example, be initiated by an electromagnet acting on a permanent magnet loading a flexible beam [21,34]. Another practical way is to use the piezoelectric itself for this purpose, which can be loaded by applying an external voltage source to it. However, the functioning of the impulse initiating system is not the subject of this paper. The article presents exemplary results of model tests, confirming the possibility of influencing the solution by means of an impulse, and thus increasing the efficiency of harvesting energy. To determine the optimal moment of impulse initiation, a numerical procedure was developed which illustrates the results of computer simulations in the form of a multi-colored diagram of impulse excitation.

2. Formulation of the mathematical model

The subject of modelling is the QZEH energy harvesting system (*Quasi-Zero Energy Harvester*), in which the potential barrier was mapped with the quasi-zero stiffness characteristic. In comparison to other design solutions, based on a flexible beam and permanent magnets, the system proposed here is characterized by an almost flat energy potential well. To clearly explain the schematic diagram, the phenomenological model is presented in two views (Fig. 1). The quasizero stiffness subsystem (Fig. 1b) represents the view from the right and provides an opportunity to identify the mechanical characteristics of the system. The model tests assumed a symmetrical structure of connections of elastic elements, which are fixed at points *A, B* and *C* to the non-deformable frame *IV*. The system is rigidly attached to the machine component by means of the screws *III*. The piezoelectric element *II* is glued to the surface of the flexible beam *I*, which under the influence of external forces undergoes elastic deformation. As a result of the beam deformation on the piezoelectric electrodes, an electric charge is induced. It was assumed that the inertial element m can move along the straight line, of which, direction is determined by points *B* and *G* of the main spring mounting c_1. This assumption determines the appropriate construction solutions, which are not shown in the diagram (Fig. 1a). At this point, we only indicate that the inertial element m is connected to the flexible beam *I*, via the hinge *H* and a movable link that moves parallel to the base of the frame *IV* inside the inertial element *m*.

The potential barrier is unequivocally defined by the main spring c1 and two compensation springs c_2 and c_3, which are incidental with the inertia element m. We assume that the stiffnesses of the compensation springs c_2 and c_3 have the same values. In the position of static equilibrium, the elastic elements c_2 and c_3 are oriented parallel to the base of the rigid frame *IV*. The b_Z energy dissipation element additionally model's energy losses in the joints of the compensation springs. Based on the presented phenomenological models, the differential equations of motion reflecting the dynamics were derived, the mechanical characteristics of the quasi-zero stiffness system were identified, and the differential equations of motion were derived.

2.1. Identification of the mechanical characteristics of the quasi-zero stiffness system

Based on the adopted phenomenological model (Fig. 1b), which demonstrates the cause-and-effect relationship between the displacement q of the inertial element and the external load F. Neglecting the influence of inertia and dissipation forces, the load F is balanced by three forces induced in the main spring c_1 and two compensation springs c_2, c_3 – assuming that c_3 equals c_2:

$$F(q) = F_1 + 2F_2 sin\varphi = c_1 q + 2(F_{20} + c_2 \Delta L)\frac{q}{\sqrt{a_0^2 + q^2}}, \quad a_0 > 0 \, . \tag{1}$$

In equation (1), the value F_{20} represents the preload of the compensation springs. Appropriate analytical relationships are derived from the reference system, the beginning of which is located at point *A* (Fig. 1). The lengths of the compensation springs in the position of static

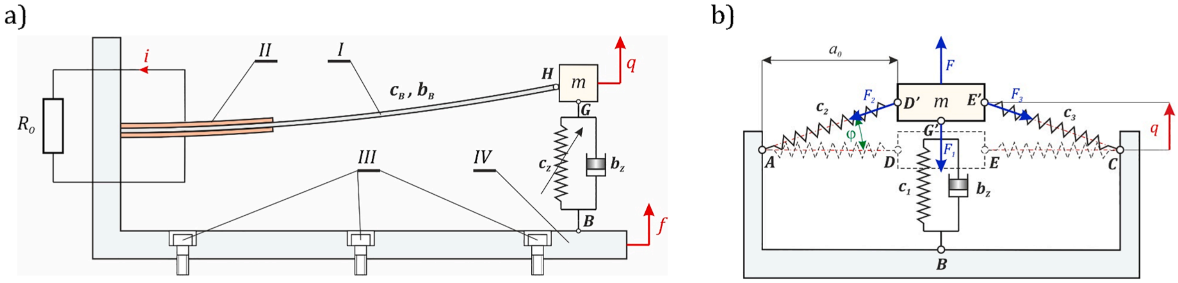

Fig. 1. Idea diagrams: (a) phenomenological model of the energy harvesting system, (b) quasi-zero stiffness system.

equilibrium $\|\boldsymbol{AD}\|$, after their deformation $\|\boldsymbol{AD}'\|$ and the size characterizing their shortening or elongation ΔL are given by the equations:

$$\|\boldsymbol{AD}\| = \sqrt{a_0^2}, \quad \|\boldsymbol{AD}'\| = \sqrt{a_0^2+q^2}, \quad \Delta L = \|\boldsymbol{AD}'\| - \|\boldsymbol{AD}\|. \tag{2}$$

Bearing in mind the fact that the quasi-zero stiffness system is characterized by a symmetrical configuration of the springs $c_3 = c_2$, it is enough to define the relationship that defines the change in length with respect to one spring. After combining equation (2) with equation (1), we obtain the equation for the static characteristics of the system with quasi-zero stiffness:

$$F(q) = c_1 q + 2\left(F_{20} + c_2\left(\sqrt{a_0^2+q^2} - \sqrt{a_0^2}\right)\right)\frac{q}{\sqrt{a_0^2+q^2}}. \tag{3}$$

The proper functioning of the system and the ensuring of a flat energy potential well, depends on the selection of the appropriate initial tension of the F_{20} compensation springs. In order to identify the appropriate initial tension, equation (3) is differentiated with respect to the generalized coordinate:

$$c(q) = \frac{\partial F(q)}{\partial q} = c_1 + \frac{2c_2q^2}{a_0^2+q^2} - \frac{2q^2\left(F_{20} + c_2\left(\sqrt{a_0^2+q^2} - \sqrt{a_0^2}\right)\right)}{\left(\sqrt{a_0^2+q^2}\right)^3} + \frac{2\left(F_{20} + c_2\left(\sqrt{a_0^2+q^2} - \sqrt{a_0^2}\right)\right)}{\sqrt{a_0^2+q^2}}. \tag{4}$$

Considering zero or close to zero stiffness of the quasi-zero stiffness system, equation (4) equates to zero $c(q=0) = \frac{\partial F}{\partial q} = 0$, and also assumes zero displacement of the inertial element $q = 0$. After considering the above assumptions, the tension of the compensation springs takes the form:

$$F_{20} = -\frac{c_1\sqrt{a_0^2}}{2}. \tag{5}$$

Finally, the mechanical characteristic describing the relationship between the deflection q and the external load F is given by the equation:

$$F(q) = \underbrace{(c_1 + 2c_2)}_{c_Z}\left(1 - \frac{\sqrt{a_0^2}}{\sqrt{a_0^2+q^2}}\right)q \tag{6}$$

Also, the form of the energy potential is obtained as a result of integrating the mechanical characteristics (5):

$$V(q) = \int F(q)dq = \frac{c_Z}{2}\left(a_0 - \sqrt{a_0^2+q^2}\right)^2. \tag{7}$$

The relationship (7) clearly indicates that the potential function is influenced by two parameters. One of them is the equivalent stiffness c_Z, the increase of which, limits the zone in which the energy potential is close to zero (Fig. 2b). On the other hand, the second is the geometric quantity a_0, which causes the well to flatten as the value increases (Fig. 2b)

The identified static characteristics of the quasi-zero stiffness system constitute the formal basis for quantitative and qualitative modelling tests.

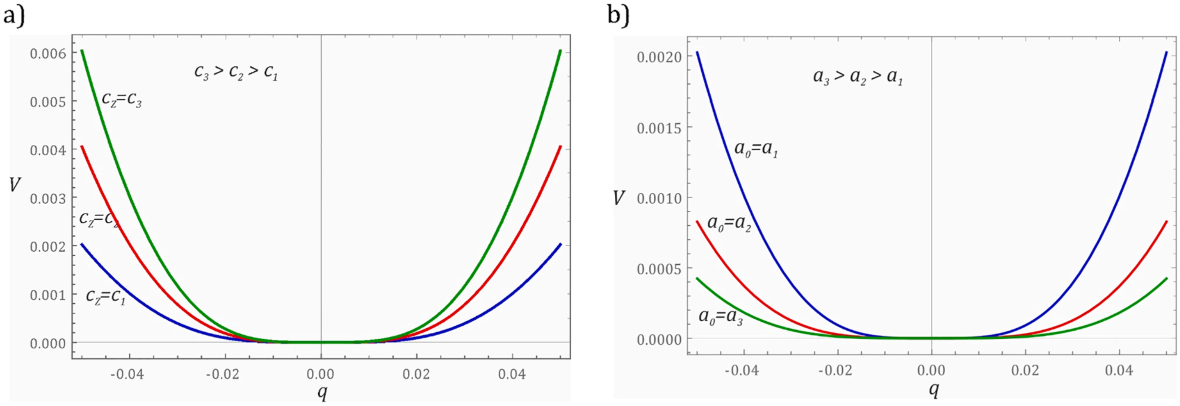

Fig. 2. Results of numerical calculations showing the influence of the mapping parameter: (a) equivalent stiffness c_Z, (b) distance a_0.

2.2. Formulation of a dimensionless model

From a mathematical point of view, the energy dissipation elements b_B and b_Z (Fig. 1) form a parallel connection. For this reason, a simplification has been made, which boils down to the derivation of the dissipative element $b = b_B + b_Z$. The situation is similar to the elastic element modelling the stiffness of the c_B beam and the main spring c_1. Because of this simplification, it is necessary to increase the stiffness c_1 by the value c_B. The system is influenced by a periodic kinematic excitation, which is a superposition of two harmonic functions: $f = A_1 sin(\omega_1 t) + A_2 sin(\omega_2 t)$.

We assume that the amplitudes of individual excitations have the same values $A_1 = A_2 = A$, which can be considered a simplification. Nevertheless, mapping the mechanical vibrations much better imitates reality than the harmonic excitation, which is usually adopted in simulation studies. The decision to load the system in such a way was due to the fact, that mechanical vibrations, induced by technical devices, can be described only in rare cases by using a simple harmonic function. Two-frequency excitation was considered in the study [35], where the phenomenon of vibration resonance was also considered.

Considering the adopted model and simplifying assumptions, the differential equations of motion of the tested system take the form:

$$\begin{cases} m\dfrac{d^2q}{dt^2}+b\left(\dfrac{dq}{dt}-\dfrac{df}{dt}\right)+c_Z\left(1-\dfrac{a_0}{\sqrt{a_0^2+(q-f)^2}}\right)(q-f)+k_PU_P=0,\\ C_P\dfrac{dU_P}{dt}+\dfrac{1}{R_O+R_P}U_P-k_P\left(\dfrac{dq}{dt}-\dfrac{df}{dt}\right)=0.\end{cases} \tag{8}$$

The coefficients in the mathematical model (8) represent respectively: constant k_P, capacitance C_P and resistance R_P of the piezoelectric. The R_O parameter is used to reproduce a system powered by energy harvested from the mechanical vibrations. Because of the efficient and effective numerical tests, the system of equations (8) can be considered in a dimensionless form. For this purpose, we introduce a new variable, defined as the difference of displacements of the inertial element m and the external kinematic input $y = q - f$, where the new variable depends on the dimensionless time $\tau = \omega_0 t$.

$$\begin{cases} \dfrac{d^2x}{d\tau^2}+\delta\dfrac{dx}{d\tau}+\left(1-\dfrac{1}{\sqrt{1+x^2}}\right)x-\theta U_P=\omega^2p\left(sin(\omega\tau)+\mu^2 sin(\mu\omega\tau)\right),\\ \dfrac{dU_P}{d\tau}+\sigma U_P+\vartheta\dfrac{dx}{d\tau}=0.\end{cases} \tag{9}$$

where:

$$\omega_0^2=\frac{c_Z}{m},\quad \delta=\frac{b}{m\omega_0},\quad \theta=\frac{k_P}{ma_0\omega_0^2},\quad p=\frac{A}{a_0},\quad \mu=\frac{\omega_2}{\omega_1},\quad \omega=\frac{\omega_1}{\omega_0},$$

$$x=\frac{y}{a_0},\quad \vartheta=\frac{k_Pa_0}{C_P},\quad \sigma=\frac{1}{\omega_0C_PR_Z}.$$

Numerical simulations will be carried out using the mathematical model of the energy harvesting system with an almost flat energy potential well, formulated in this way.

Table 1
Geometric and physical parameters of the model.

Name	Symbol	Value
Inertial element (mass) loading the beam	m	0.02 kg
Energy losses in a mechanical system	b_B	0.02 Nsm^{-1}
Equivalent stiffness of a quasi-zero system	c_Z	18 Nm^{-1}
Length of the compensation springs in the equilibrium position	a_0	0.03 m
Equivalent resistance of the electrical circuit	R_Z	$1.1\cdot10^6$ Ω
Equivalent capacity of the electric circuit	C_P	72 nF
Electromechanical constant of piezoelectric converter	k_P	$3.985\cdot10^{-5}$ N/V

3. Results of numerical simulations

Model studies, mapping the dynamics of the energy harvesting system with quasi-zero energy potential, were carried out with reference to the numerical data from the tested system, which is summarized in Table 1.

Based on the numerical data characterizing the mathematical model, numerical tests were carried out, showing the effect of the dimensionless frequency ω of the excitation and selected physical quantities on the location of chaotic motion zones. Many methods are used for such an assessment, however, the most frequently used is the largest Lyapunov exponent λ [36,37]. Using the selected cross-sections of multi-coloured λ distribution maps, the efficiency of energy harvesting was estimated, and diagrams of coexisting solutions were drawn.

3.1. Distribution of the Lyapunov exponent and the effectivity of energy harvesting

During the identification of the largest Lyapunov exponent, a three-dimensional phase space was assumed $(x, \dot{x}, U_P)$. All the multi-colored maps of the λ distribution were plotted for zero initial conditions $x(0) = 0, \dot{x}(0) = 0, U_P(0) = 0$. In an attempt to obtain a satisfactory resolution, the range of variability of the control parameters defining the abscissa and ordinates was divided into 500 intervals. To identify λ, the numerical algorithm proposed by Wolf (Wolf et al. 1985) was implemented in the phase space spanning the computed coordinates. When plotting multi-colored maps, two control parameters p and ω were chosen, characterizing the external source of excitation, and the initial distance between the tested trajectory and the reference trajectory was assumed to be $\varepsilon(0) = 10^{-5}$. Positive values of λ indicate chaotic behavior, otherwise the phase trajectories tend to be stable points or periodic orbits. On the other hand, when λ takes values equal to zero, we deal with the so-called bifurcation points. Technically, the mechanical properties of the *QZEH* system are determined by the equivalent stiffness c_Z and the mass m applied at the end of the flexible beam. The exemplary results illustrating the influence of mechanical quantities on the distribution map of the largest Lyapunov exponent are presented in the graphs (Fig. 3). The results of computer simulations were limited to the case when harmonic vibrations affected the energy harvesting system $\mu = 0$.

We assume that the geometrical dimensions of the system and the mass loading the free end of the flexible beam remain unchanged (Table 1). However, we modify the stiffness of the system, then with an increase in the value of c_Z, the area of chaotic solutions increases (Fig. 3). In the conducted tests, the expansion of the unpredictable solutions zones is determined by the equation defining the dimensionless damping coefficient δ. An increase in the equivalent stiffness c_Z increases the dimensionless frequency ω_0 occurring in the denominator, which consequently leads to a decrease in the value of the dimensionless damping.

Then, the influence of the parameter μ, which defines the relationship between the frequencies of individual harmonic components on the distribution of the largest Lyapunov exponent λ, was examined. The results of the numerical experiments were also visualized in the form of two-dimensional multi-colored maps, which were plotted in relation to selected values of the parameter μ. The overriding goal of this study is to evaluate the effectivity of energy harvesting. For this reason, the RMS value of the voltage induced on the piezoelectric electrodes was adopted as an indicator [38,39]. The results of the numerical test are presented in the form of diagrams, drawn in relation to the arbitrarily selected values of the control parameter p. The multi-colored maps of the largest Lyapunov exponent clearly show the influence of the frequency ratio μ on the location of the zones of chaotic solutions. It is also worth noting that

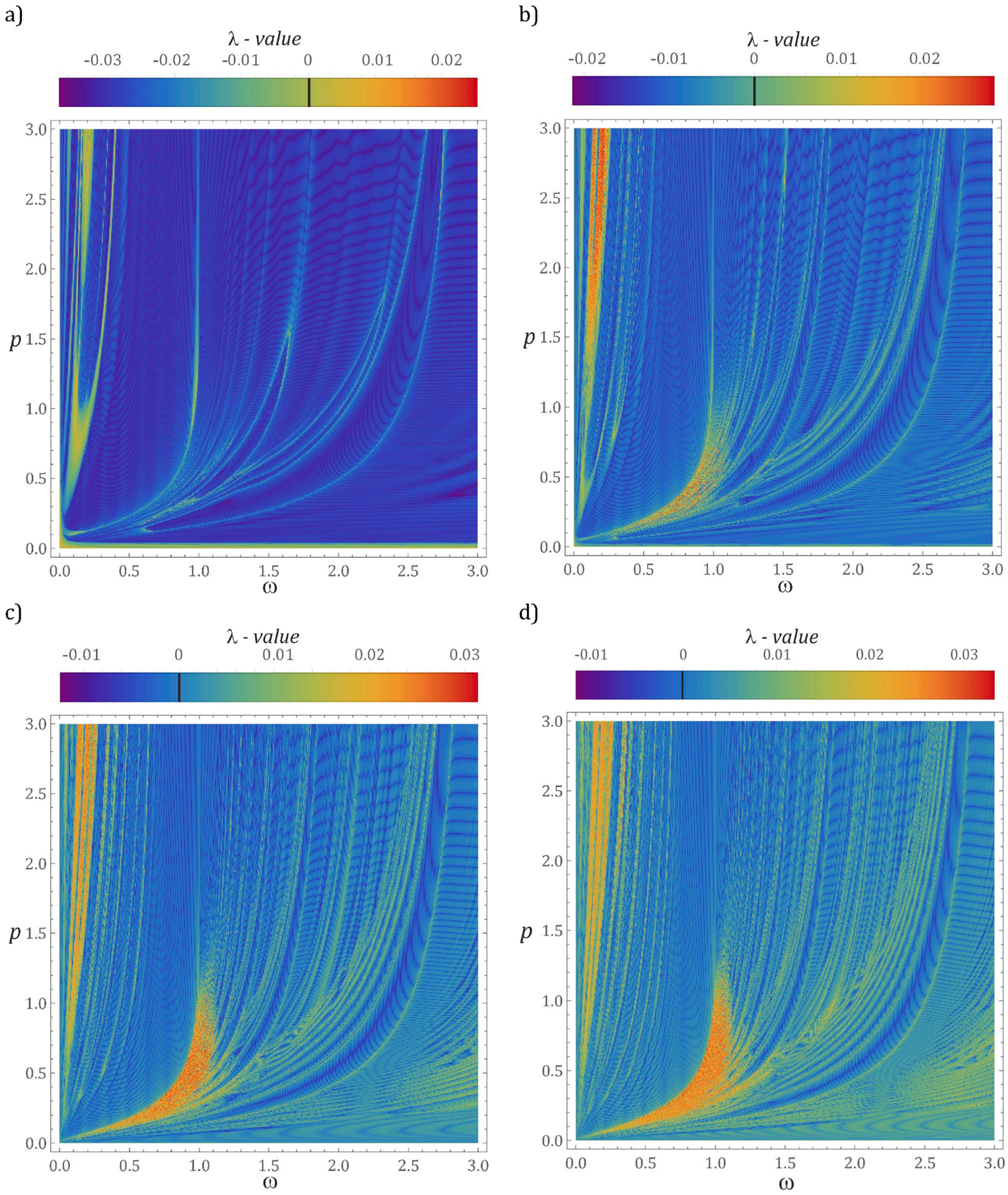

Fig. 3. Influence of the stiffness c_Z on the distribution of the largest Lyapunov exponent: (a) $c_Z = 4.5$, (b) $c_Z = 18$, (c) $c_Z = 72$, (d) $c_Z = 144$. Zero initial conditions were used for the simulation.

there is a direct correlation between the Lyapunov map and the RMS voltage diagram. Selected examples corresponding to the μ coefficient, assuming values from the set of integers, reciprocals of integers and rational and irrational numbers are illustrated in the graphs (Fig. 4).

When μ takes values from the set of integers or their reciprocals, then periodic solutions dominate the image of the largest Lyapunov exponent. In a situation where μ is determined by a rational or irrational number, the zones of unpredictable solutions are activated.

In the graph (Fig. 4d) the points on the multi-colored map of the largest Lyapunov exponent are not located directly on the border of the periodic and chaotic solutions zone. This is due to the accuracy of the identification of the Lyapunov exponent, the value of which was estimated, based on a very short time sequence. Based on the graphs (Fig. 4), it can be concluded that the local maximums of the diagram of RMS voltage values correspond to the dimensionless frequency, beyond which unpredictable solutions dominate. This is also the point where energy harvesting efficiency drops sharply. When the Lyapunov exponent takes the values $\lambda \approx 0$, there is a minimum voltage drop in the diagram of the RMS voltage. This situation is very well illustrated by the graph (Fig. 4b), unmarked points on the dashed line $p = 0.4$, between $X_4^{'}$ and $Y_4^{'}$. An analogous situation takes place in the sections determined by the values of the control parameter $p = 0.3$ and $p = 0.2$. It is worth noting that regardless of the characteristics of the external input source, in the

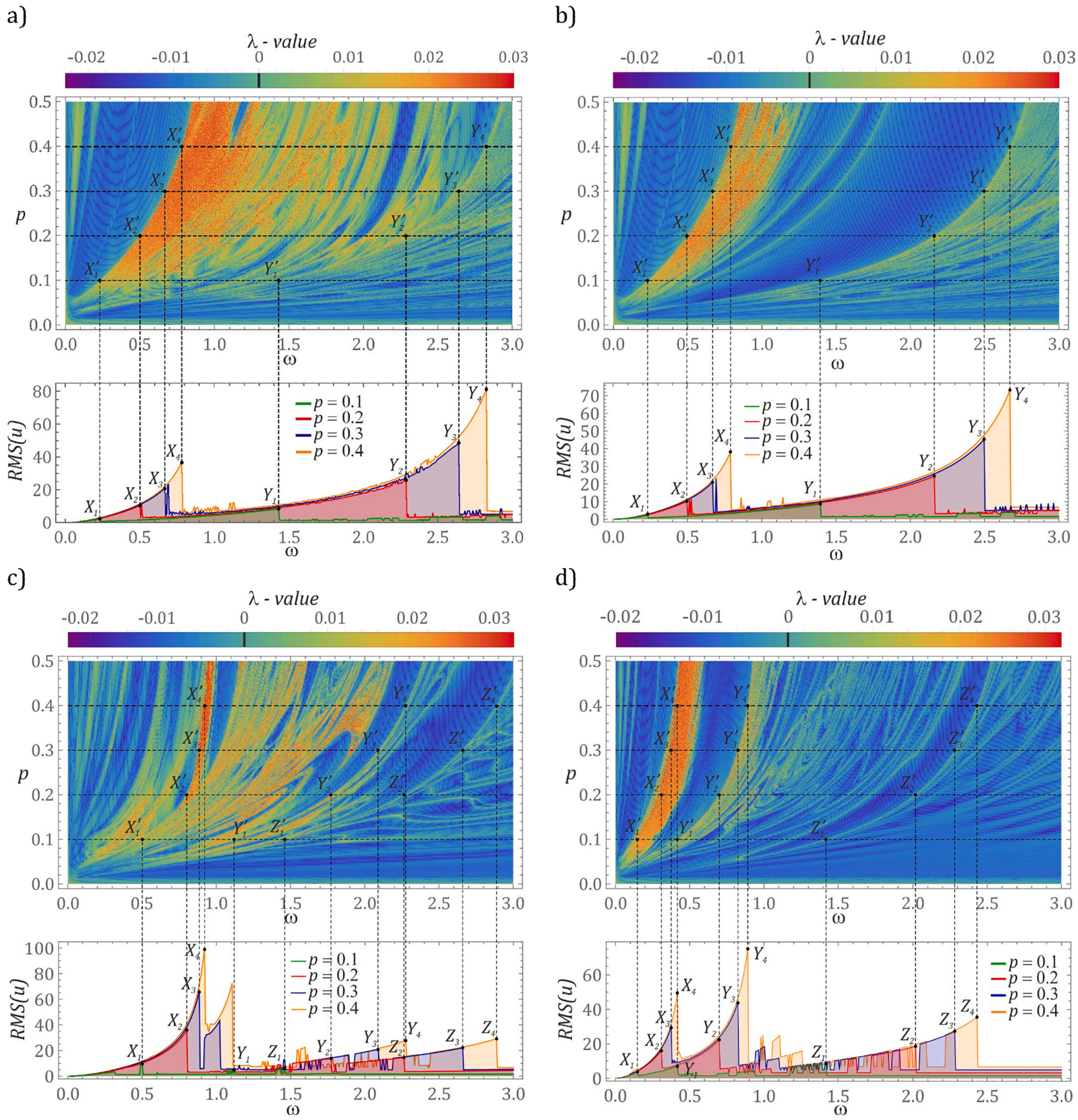

Fig. 4. Energy effectivity diagrams. The exponent λ and RMS(u) as a function of the frequency ω and the control parameter p for different values of μ: (a) $\mu = \frac{1}{\pi}$, (b) $\mu = \frac{1}{3}$, (c) $\mu = \frac{4}{5}$, (d)$\mu = 2$ Zero initial conditions were used for the simulation.

zones of periodic solutions $\lambda < 0$, a higher voltage is induced on the piezoelectric electrodes. Moreover, a direct comparison of the diagrams of the RMS voltage value with the multi-colored maps of the distribution of the largest Lyapunov exponent confirms the hypothesis that the increase in the value of μ coefficient causes the characteristic curves to shift towards lower frequencies.

If the system is affected by mechanical vibrations, and the ratio of the harmonic frequencies is given by an irrational number $\mu = \frac{1}{\pi}$ (Fig. 4a), then the most energy is harvested when the dimensionless frequency is in the vicinity of the point Y_4 ($\omega = 2.8$). In the range of lower values of ω, the local maximum of the RMS diagram corresponds to the frequency $\omega \approx 0.8$ (point X_4). The mentioned values correspond to the case when the system is influenced by external mechanical vibrations with the amplitude $p = 0.4$. As the p-value is reduced, less voltage is induced at the piezoelectric electrodes, while local maxima are shifted towards lower ω values.

A very similar situation occurs when the system is affected by external excitations, for which the coefficient μ takes the value of the reciprocal of an integer (Fig. 4b). While in the range of low values of ω, it is not possible to show significant differences. In the frequency band $\omega > 2$ the maximum of the diagram of RMS voltage values is shifted to the left. With reference to the presented examples, the highest RMS voltage values were recorded when the coefficient μ takes a value from the set of rational numbers (Fig. 4c). In the case of (Fig. 4d), the diagrams of RMS voltage values are characterized by a much larger number of local maxima. In the studied range of variability of the control parameter p, the position of the points $X_i^{'}, Y_i^{'}, Z_i^{'}$ can be approximated with high accuracy by the exponential function.

The results of the numerical tests presented in the graphs (Fig. 4) show only a pictorial of the relationship between the effective value of the voltage induced on the piezoelectric electrodes and the largest Lyapunov exponent. In addition, the energy efficiency diagram was plotted assuming zero initial conditions. Considering the quantitative and qualitative assessment of the impact of the coefficient μ, defining the

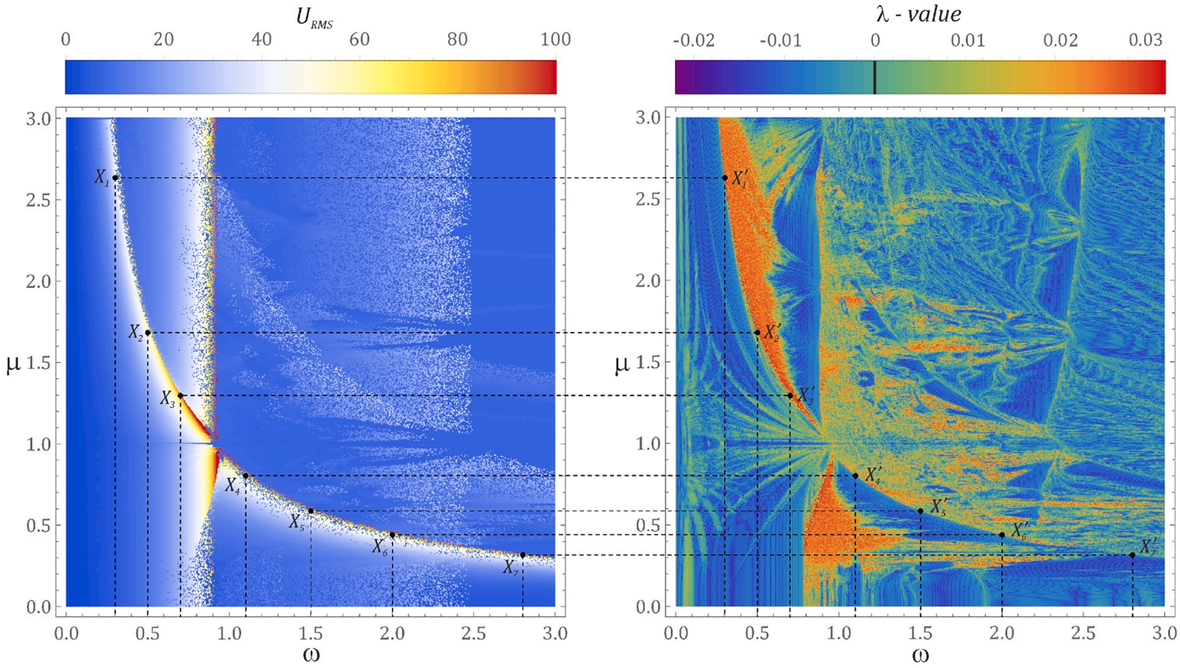

Fig. 5. Maps of the output voltage and the Lyapunov exponent as a function of μ and ω obtained for zero initial conditions. It is worth paying attention to the correlation of jump changes in contrasts on the map λ with U_{RMS} maxima.

ratio of the frequency of the external excitation affecting the system, multi-colored maps of the largest Lyapunov exponent and the RMS value of the induced voltage were drawn (Fig. 5). The multi-colored effective voltage map was generated assuming randomly changing initial conditions. This approach to the numerical experiments takes into account coexisting solutions, and ultimately determines the optimal operating conditions of the energy harvesting system with quasi-zero stiffness.

As in the case of the tests carried out with the assumption of zero initial conditions, the obtained results clearly indicated the limitation of the energy recovery capacity if the operating point of the system was in the chaotic zone. Based on the multi-colored map of the RMS voltage, it is possible to demonstrate the system's negligible ability to harvest energy in the range of low values of the dimensionless frequency $\omega \in [0, 0.2]$. The situation is slightly better for the higher values of the excitation frequency $\omega > 2.5$, because at this frequency, it is possible to distinguish ranges of variability of the μ coefficient, for which the effective value of the voltage induced on the piezoelectric electrodes reaches the value in the range $U_{RMS} \in [30, 50]$ ($\mu \in [0.4, 0.5]$ and $\mu \in [0.6, 0.8]$). It is also worth noting that for $\mu = 1$, the system with quasi-zero stiffness does not meet the expectations set for it.

Energy is most efficiently harvested when the operating point is located just before the "fault". The course of one of these (energy-efficient) "faults" is marked with the symbols denoted by X_i. Its course can be accurately approximated by the power function, given by the equation $\mu = 0.866\omega^{0.961}$. The statement regarding the high accuracy is justified as the coefficient of determination has the value $R^2 \approx 0.998$. The second "fault", characterized by a similar energy effectivity, takes the form of a line running perpendicular to the ordinate axis for $\mu > 1$.

Model studies were also conducted to assess the efficiency of obtaining energy from coexisting solutions, these are documented later in this paper.

3.2. Multiple solutions identification

One of the characteristic properties of nonlinear dynamical systems is related to the coexistence of several solutions. From the numerical point of view, this problem comes down to the study of many steady-state trajectories, the beginnings of which are in different places of the phase plane. For this purpose, a numerical procedure was developed in Wolfram Mathematica software, through which it is possible to estimate the number and periodicity of coexisting solutions *DS – Diagram of Solutions*. The results of numerical calculations were visualized in the form of a graph with the following diagrams: DPS – Diagram of Periodic Solutions (blue points) and DNS – Diagram of Number Solutions (blue shaded diagram). At this point, we indicate that the procedure for drawing DPS and DNS diagrams is based on the fixed points of the Poincare cross-section. It should be noted that the above-mentioned diagrams are used for the initial assessment of the nature of coexisting solutions, because their accuracy is a compromise between the precision of numerical calculations and the time of computer simulation. For this reason, tests with higher levels of precision are carried out in relation to specific values of the parameter ω. The following diagrams of coexisting solutions are plotted for 300 different values of the control parameter ω. Moreover, in view of the possibility of assessing the variability range of ω, they were compared to the diagrams of the effective value of the voltage induced on the piezoelectric electrodes. The energy effectivity charts were produced using randomly selected initial conditions.

Coexisting multiple solutions identified for selected values of the dimensionless frequency ω, located in the zone between "faults" X_1 and X_2, were identified after 500 periods of the external force had been applied. On the other hand, the Poincare cross-section points, based on which the periodicity of the solution was defined, were determined, based on a time window of 50 periods of the external load. The results of the model tests were visualized in the form of basins of attraction and pie charts, which contain basic information characterizing the identified solution. However, in view of the possibility of a direct reference of the basin of attraction to a specific solution, the colors contained in the pie charts were correlated with the colors of the basins of attraction. The probabilities A of the occurrence of a given solution were estimated by counting the initial conditions, corresponding to a given attractor.

Periodic solutions dominate the studied range of ω variability. It is worth noting that the number of edges of the U_{RMS} diagram correlate with the number of coexisting solutions in the *DS* diagram. (Fig. 6). It should be noted that the accuracy of the identification of the edges of the energy effectivity diagram (U_{RMS}) is significantly dependent on the number of initial conditions included in the plot. Until the first "fault" X_1

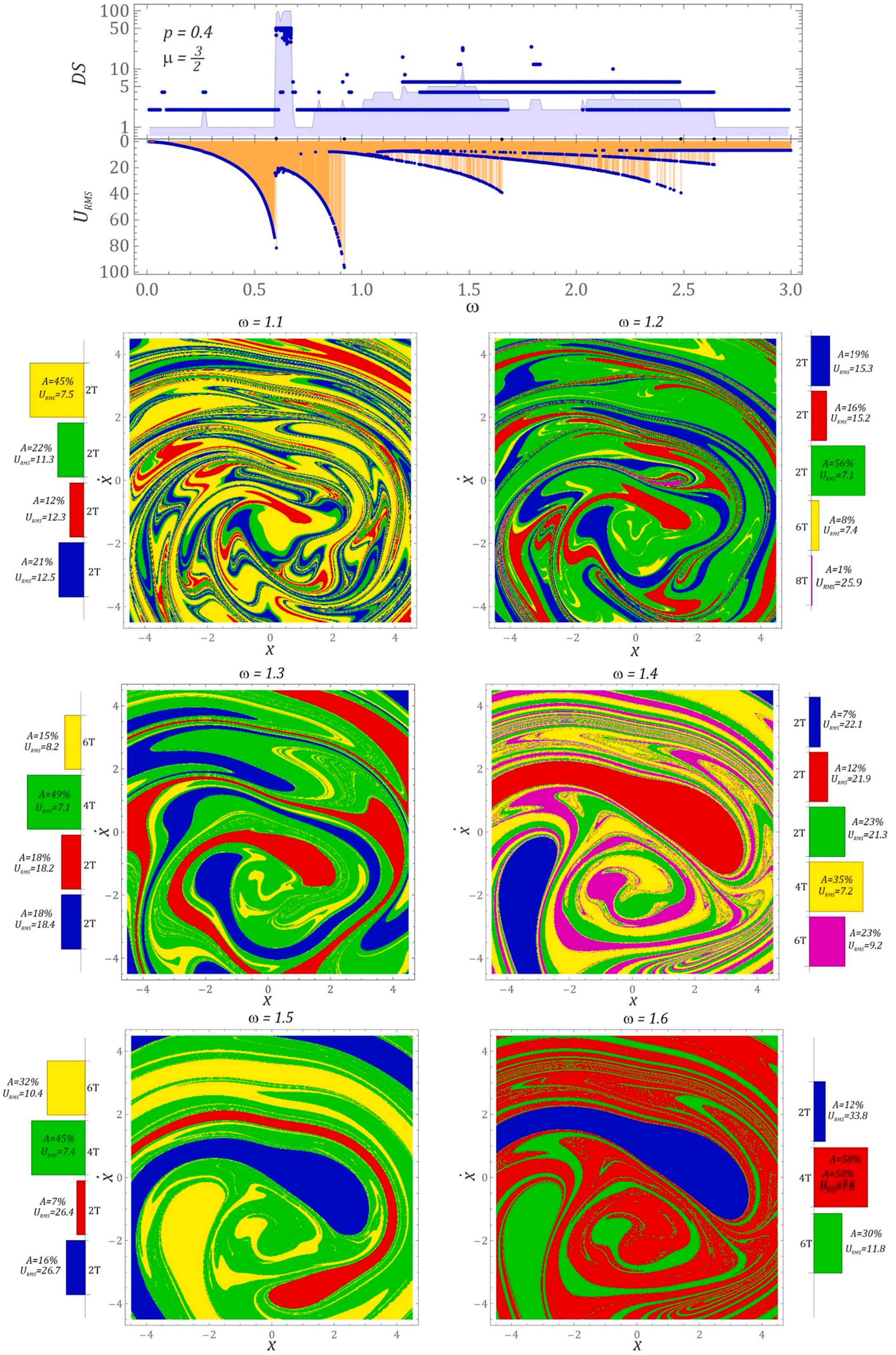

Fig. 6. Sample graphic images of basins of attraction of coexisting solutions. Bar graphs show the contribution of individual solutions $\mu=3/2$. The fractal form of the basins of attraction implies chaotic solutions. In simulations, the value of $U_p = 0$ for $t = 0$.

appears, there is basically a single periodic solution with a periodicity of *2T*, which is determined by the denominator of the μ coefficient. It is the lowest periodicity that occurs in the analyzed range of ω. The periodicity of the remaining solutions most often assumes values that are multiples of *2T*. After passing through the "fault" X_1, the system response takes the form of chaotic solutions, and the effectiveness of energy harvesting decreases rapidly. Such solutions occur in a relatively narrow range of variability of the control parameter $\omega \in [0.6, 0.7]$. We deal with double periodic solutions with *2T* periodicity in the range $\omega \in [0.8, 1]$. Nevertheless, in the middle of this range there is a "fault" X_2 ($\omega \approx 0.91$), the consequence of which is a significant limitation of energy harvesting. With three and four coexisting solutions with *2T* periodicity, we deal with the variability range $\omega \in [1.1, 1.17]$. In the band $\omega \in [1.2, 2.65]$ there are solutions whose periodicity is a multiple of *2T*. In the zone $\omega \in [1.7, 2.05]$ the system response may take the form of vibrations with periodicity of *4T* and *6T*. Only in the vicinity of the frequency $\omega \approx 1.8$, solutions with *4T, 6T* and *12T* periodicity coexist. It is worth noting that in the case under consideration, the most effective energy harvesting takes place within the variability of the control parameter $\omega \in [0.4, 0.91]$. A similar efficiency of obtaining energy can be obtained for higher values of ω. Nevertheless, this is the case with specific solutions. After passing through the "fault" X_i, the number of coexisting solutions is reduced.

In the case when the parameter characterizing the frequency ratio of the external load affecting the system takes the value $\mu = \frac{4}{3}$ (Fig. 7), in the range of the dimensionless frequency $\omega < 0.7$ we are dealing with single solutions with a periodicity of 3T. The value of $\omega \approx 0.7$, defines the location of the first X_1 "fault". In the band bounded by "faults" X_1 and X_2, apart from chaotic solutions, there may also be cases of single 3T-periodic solutions. As in the case already analyzed, this is the lowest periodicity that was recorded during numerical tests. Stable coexisting periodic solutions occur in the frequency range $\omega \in [X_2, X_4]$. After ω exceeds the "fault" X_4, the motion of the flexible beam of the energy harvesting system takes the form of periodic vibrations with a periodicity of 6T. Double stable periodic solutions with 3T periodicity occur in the band $\omega \in [1.1, 1.2]$. However, in the band $\omega \in [2.35, X_4]$, the response of the system may take the form of 3T and 6T-periodicity.

A similar situation takes place regarding the results of numerical tests presented in Fig. 8. This time, until the first "fault" X_1 appears, a single stable solution with 4T periodicity dominates A relatively small decrease in the value of the coefficient μ to the value determined by the ratio 5/4 results in the band $\omega \in [X_2, X_3]$ areas of the irregular chaotic solutions becoming excited. Moreover, in contrast to the examples shown in Fig. 5 and Fig. 6, when ω exceeds the value determined by the "fault" X_3, we deal with a single stable periodic solution, and its periodicity is doubled ($\omega \approx 2.6$).

In all analyzed cases, the geometric structure of the basins of attraction resemble a vortex, the center of which is not located at the origin of the coordinate system. In addition, adjacent to the "center of the vortex", the basins of attraction essentially create regular, uniform areas that become mixed and blurred as they move away from the center of the vortex. The numerical tests carried out clearly show that regardless of the numbers that define the coefficient μ, the position of the "fault" X_2 does not change. Moreover, in the vicinity of the "faults", the geometric structures of the basins of attraction create irregular areas characterized by intense mixing. Such a situation takes place, for example, in the vicinity of the "fault" X_1 for the graphic images of the basins of attraction corresponding to the frequency $\omega = 1.1$ (Figs. 6, 7 and 8). It is worth noting that the stabilization of the number of coexisting solutions in the DS diagram, increasing the value of the dimensionless frequency ω causes the edges of the basins of attraction to form a uniform regular boundary. One deals with such a situation, for example, in the basins of attraction corresponding to the frequencies $\omega = 1.4$, $\omega = 1.5$, $\omega = 1.6$ (Fig. 7).

The numbers that define the coefficient μ affect not only the geometrical structures of the basins of attraction. These numbers also determine the periodicity of the coexisting stable periodic solutions. In particular, the denominator $\mu = \frac{m}{n}$, where *m* and *n* are any numbers from the set of integers and $n \neq m$, determines the periodicity of solutions. In all the considered cases, the smallest identified periodicity of the coexisting solutions is equal to *n*. However, the periodicity of the remaining solutions was equal to the multiple of *n*. Increasing the value of the numbers defining the frequency ratio results in the band limited by "faults" $\omega \in [X_2, X_3]$, in which areas of chaotic solutions are excited. The emergence of areas of chaotic solutions causes the emergence of local "faults" disturbing the line of the edges of the basins of attraction, which takes on a fractal structure.

The conducted numerical studies, and in particular, the reference of the effective value of the voltage induced on the piezoelectric electrodes to the size of the basins of attraction, indicate that the most energy-effective solutions do not dominate in the assessed area of the phase plane. Only in the case of $\omega = 1.2$ (Fig. 6), is there a case where the dominant basin of attraction is characterized by the best efficiency of energy harvesting. It is also worth noting that the responses of the system characterized by low periodicity are characterized by better energy efficiency compared to solutions with higher periodicity. Only in the case of the external excitation with a frequency of $\omega = 1.2$, the 8T-period solution (Fig. 6) shows almost twice the energy efficiency when compared to 2T-period solutions. Moreover, the data presented in the pie charts (Figs. 6–8) clearly indicate that with the increase of the dimensionless frequency of excitation ω, the efficiency of energy harvesting in relation to the solutions characterized by the lowest periodicity, increases. Part of this is also caused by an increase in the acceleration of mechanical vibrations affecting the energy harvesting system. In addition to the typical fractal regions at the junction of two attraction regions, signaling non-linear mixing of the two solutions, fractal compositions of three solutions, also known as Wada regions, were observed. In these areas, solutions become extremely unpredictable [5].

3.3. *The influence of impulse disturbance on the ability to harvest energy*

Presented below are the results of the numerical tests, the assessment of the impact of the impulse disrupting the nature of the solution, and thus the efficiency of energy harvesting of a system with quasi-zero stiffness. During the numerical experiments, *a priori* rectangular impulse profile was assumed. The authors realize that impulses of this shape rarely occur in practice. Nevertheless, for computer simulations, such a mapping is used, as it is the simplest form of mathematical description. The formal presentation of the computer simulation results is given as a diagram of impulse excitation (Figs. 9-12), which indicates what solution can be expected after the expiration of the transient processes, assuming that the impulse is initiated at the moment τ_0. The background colors of the mechanical vibration signal affecting the energy harvesting system shown, correlate with the colors of the basins of attraction, which are presented in section 3.2. When creating the visualizations of the individual solutions, the red color was used to represent a stable phase trajectory that is influenced by the impulse at the moment τ_0. When the trajectory is excited by an impulse, the state of the system become transient and the trajectory is outlined in grey. On the other hand, when the target trajectory is stable, after the expiration of the transient processes, it is plotted in blue. A similar convention was adopted for the Poincaré points which, in the case of primary trajectories, were marked with red markers. The blue color marks the Poincaré points of the new solutions that result from the impulse action. Additionally, the moments in which the impulse initiation and expiration take place are marked with black markers in the phase plane. The dashed curve represents the phase trajectory of the system response in the pulse duration. In the numerical experiments, it was assumed that initially, the flexible beam of the energy harvesting system is in static

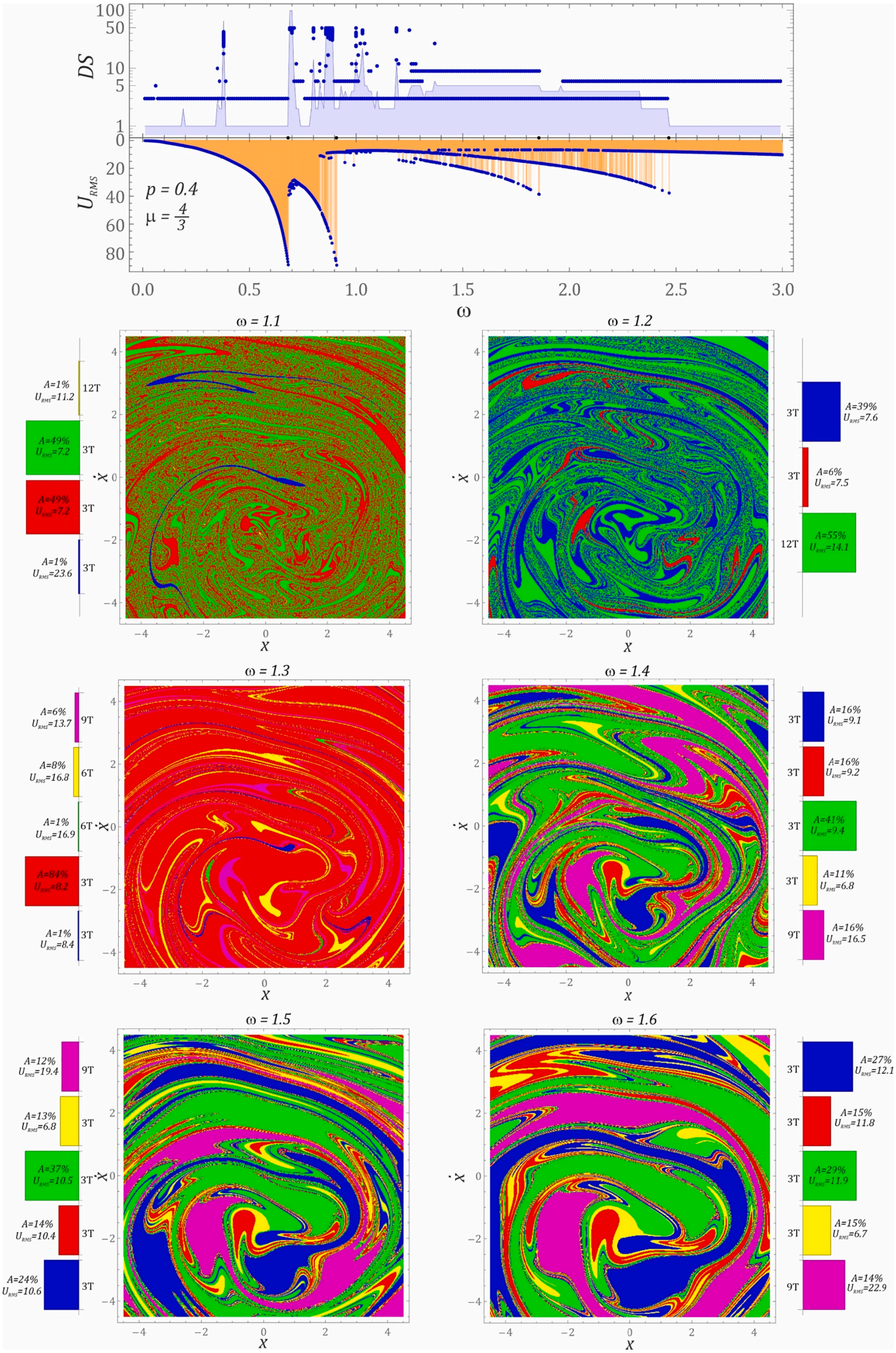

Fig. 7. Sample graphic images of basins of attraction of coexisting solutions. Bar graphs show the contribution of individual solutions μ=4/3. The fractal form of the basins of attraction implies chaotic solutions. In simulations, the value of $U_p = 0$ for $t = 0$.

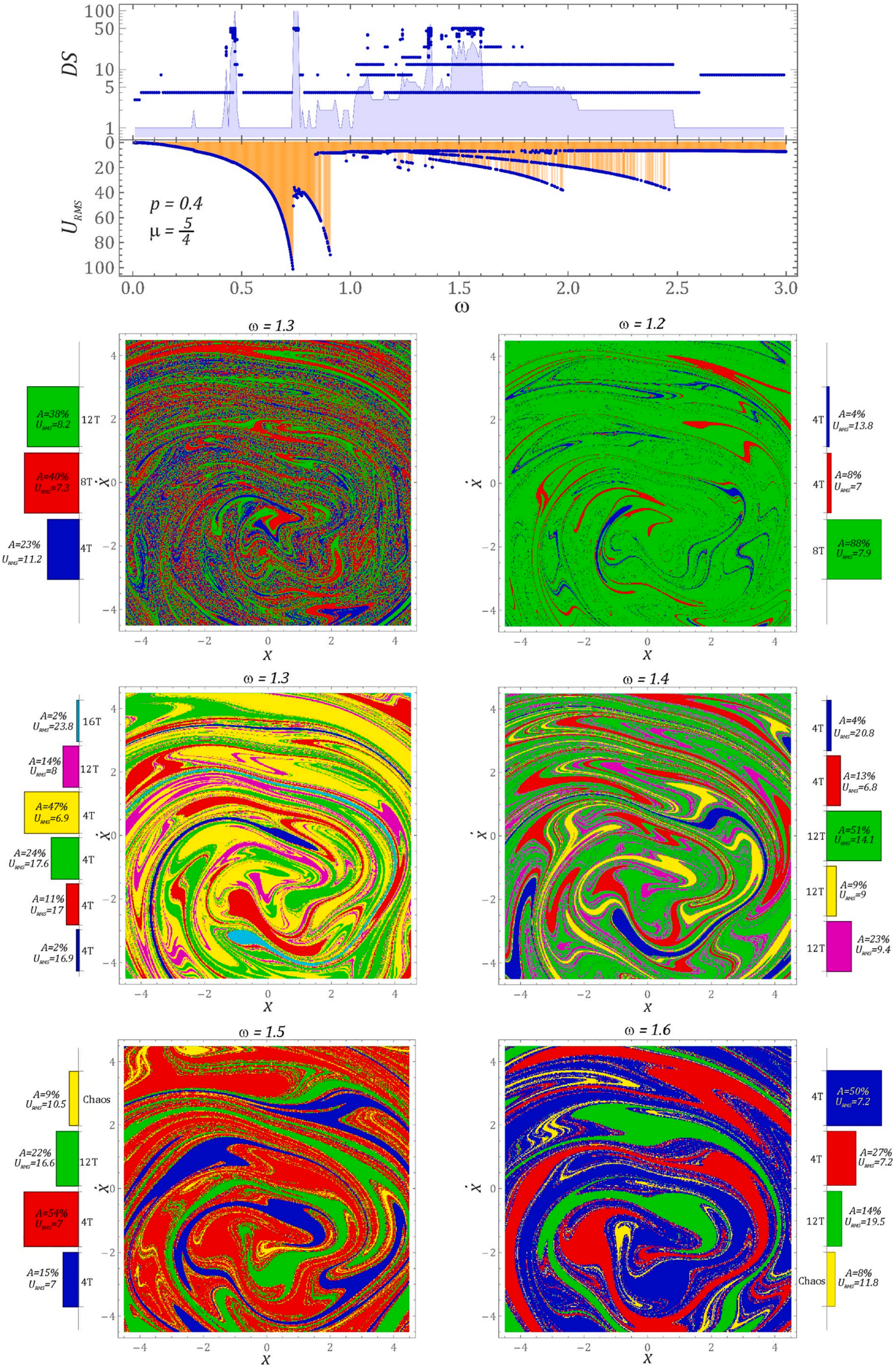

Fig. 8. Sample graphic images of basins of attraction of coexisting solutions. Bar graphs show the contribution of individual solutions μ=5/4. The fractal form of the basins of attraction implies chaotic solutions. In simulations, the value of $U_p = 0$ for $t = 0$.

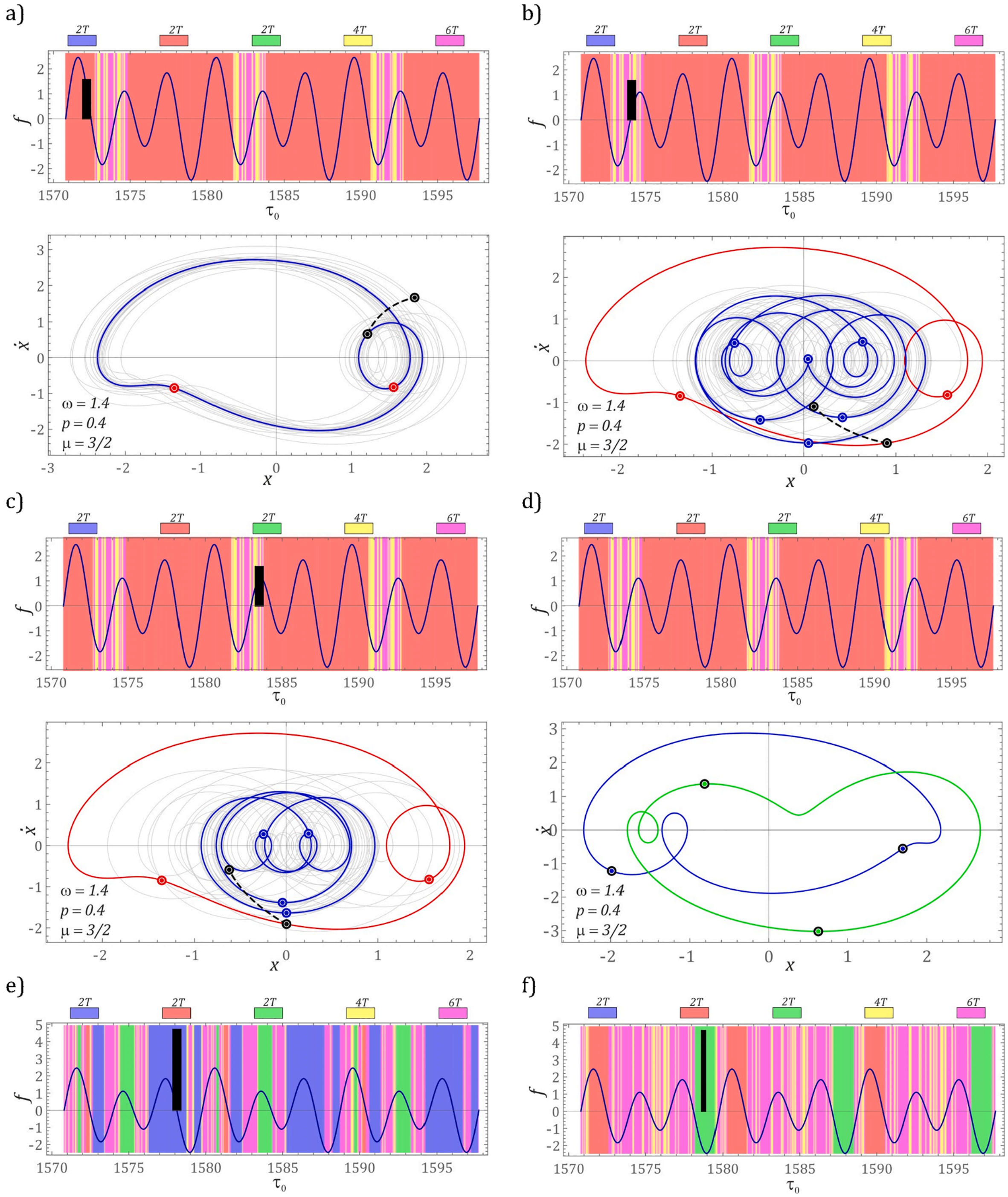

Fig. 9. Model test results: a) $\tau_0 \approx 1571.7$, $A = 2$, $\tau_1 = 0.5$, b) $\tau_0 \approx 1573.7$, $A = 2$, $\tau_1 = 0.5$, c) $\tau_0 \approx 1583.2$, $A = 2$, $\tau_1 = 0.5$, d) stable 2T-period solution $U_{RMS} \approx 22.1$ (blue basin of attraction), stable 2T-period solution $U_{RMS} \approx 21.3$ (green basin of attraction), e) $A = 6$, $\tau_1 = 0.5$, f) $A = 6$, $\tau_1 = 0.25$. (For interpretation of the references to color in this figure legend, the reader is referred to the web version of this article.)

equilibrium ($x(0) = 0$, $\dot{x}(0) = 0$). Additionally, it is assumed that the energy harvesting system is in steady state, until the impulse is initiated.

When the system is affected by an external excitation with a time response that is defined with the parameters: $p = 0.4$, $\omega = 1.4$, $\mu = 3/2$, then there are five coexisting solutions, for which basins of attraction are shown in diagram Fig. 7. In steady state, the response of the system takes the form of a 2T-periodic solution, during which the voltage $U_{RMS} \approx 12.5$ is induced on the piezoelectric electrodes. The results of the numerical experiments (Fig. 9) indicate that in the assessed time interval, the influence of the assumed impulse characteristics are not sufficient to achieve stable solutions – the phase trajectories of which are shown in the graphs (Fig. 9d). These solutions can be initiated with an impulse, but it is associated with the need to redefine its characteristics by modifying amplitude or width. The influence of the impulse characteristic on the diagrams of impulse excitation is shown in graphs Fig. 9e. The values of τ_0 dominate in the identified diagram, in which the initiated impulse allows for a 2T-periodic orbit. Its initiation in the cyclically repeating zones $\tau_0 \in [1572.7, 1574.9]$, distinguished by yellow (Fig. 9b) and magenta (Fig. 9b), results in a change in the system's response, resulting in a large decrease in energy harvesting efficiency. As part of the numerical tests, the impact of the impulse characteristics on the structure of the diagrams of impulse excitations was assessed.

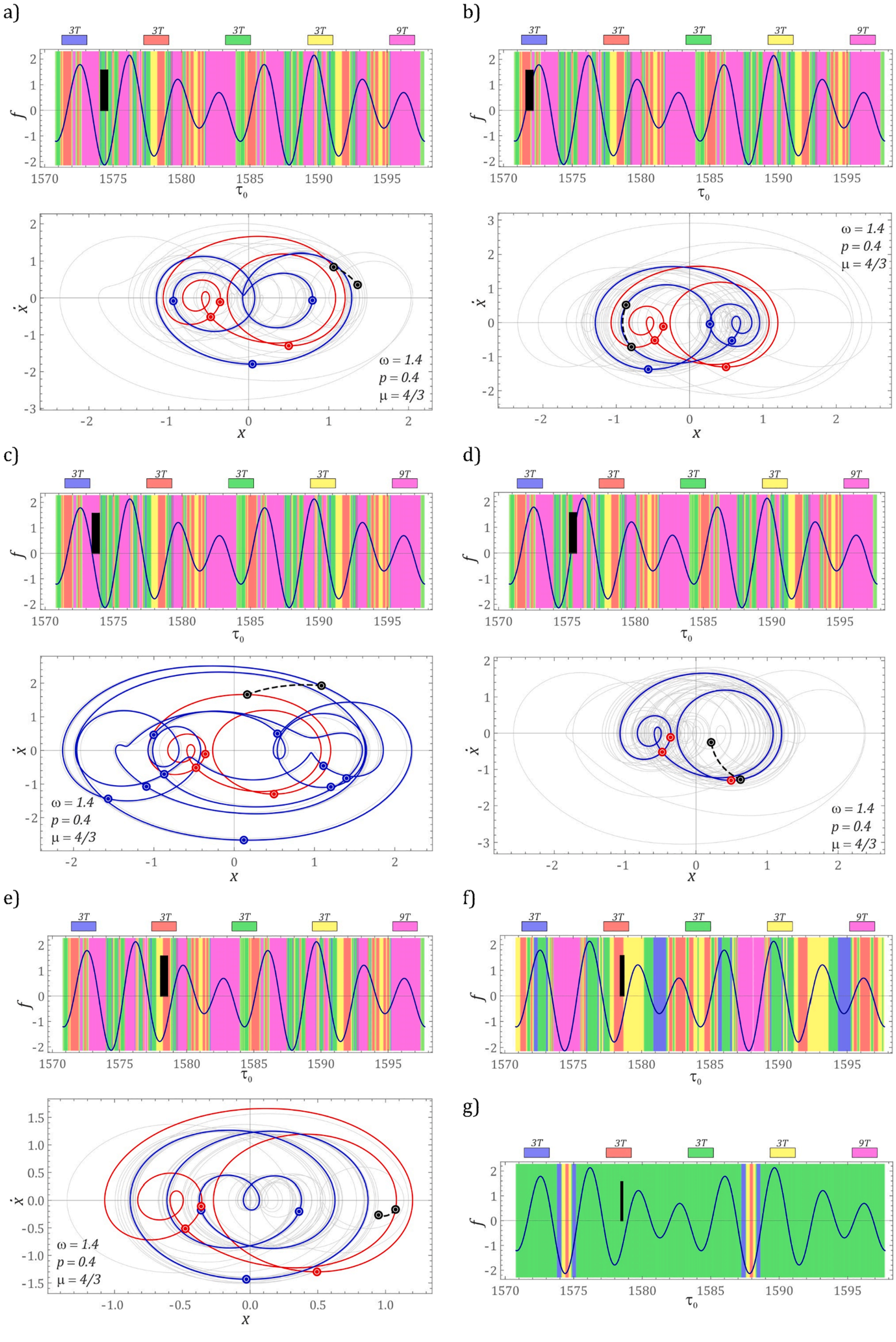

Fig. 10. Model test results: a) $\tau_0 \approx 1571$, $A = 2$, $\tau_1 = 0.5$, b) $\tau_0 \approx 1571.5$, $A = 2$, $\tau_1 = 0.5$, c) $\tau_0 \approx 1573.2$, $A = 2$, $\tau_1 = 0.5$, d) $\tau_0 \approx 1575.1$, $A = 2$, $\tau_1 = 0.5$, e) $\tau_0 \approx 1577.7$, $A = 2$, $\tau_1 = 0.5$, f) $A = 2$, $\tau_1 = 0.25$, g) $A = 2$, $\tau_1 = 0.125$.

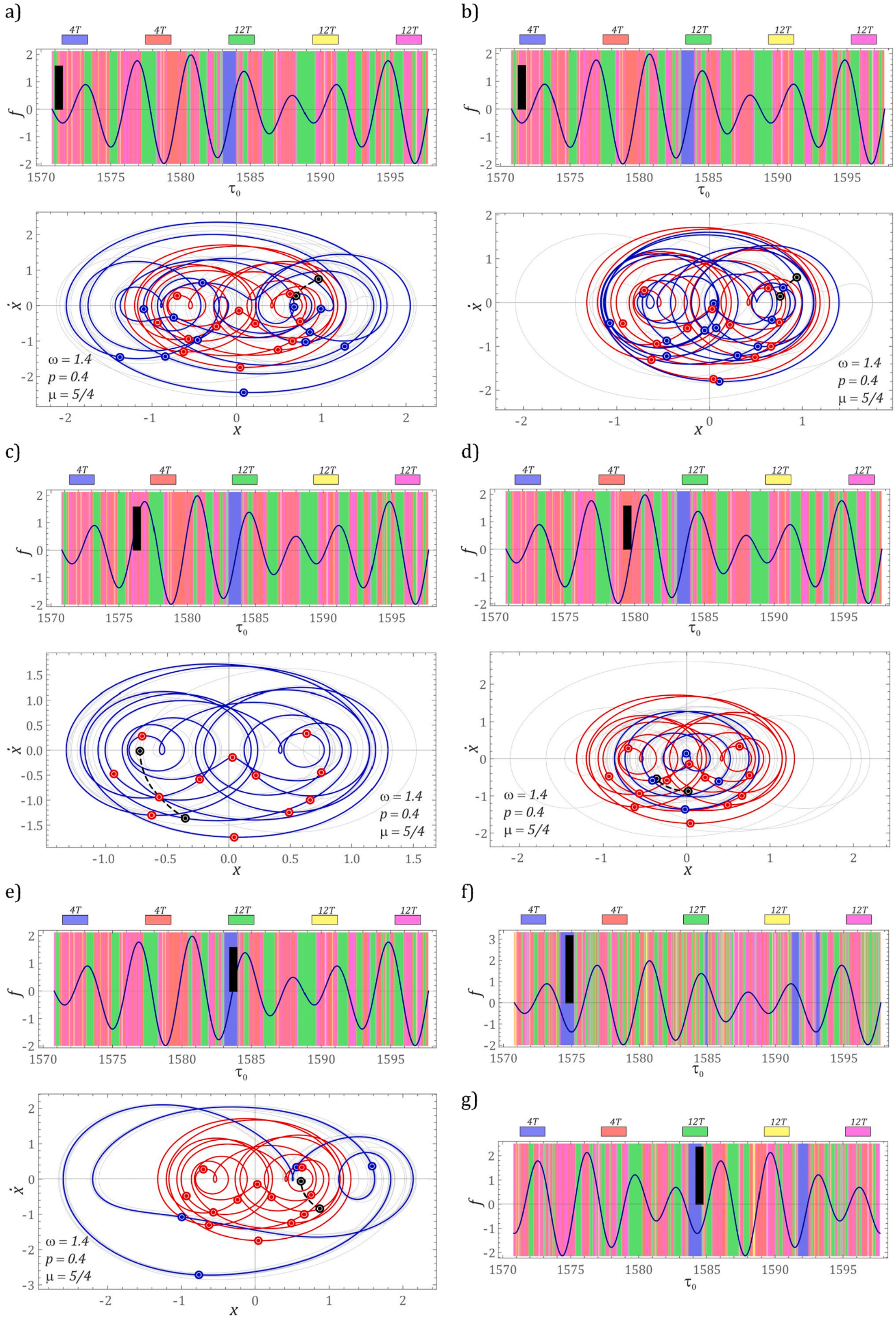

Fig. 11. Model test results: a) $\tau_0 \approx 1571$, $A = 2$, $\tau_1 = 0.5$, b) $\tau_0 \approx 1571.2$, $A = 2$, $\tau_1 = 0.5$, c) $\tau_0 \approx 1576$, $A = 2$, $\tau_1 = 0.5$, d) $\tau_0 \approx 1579.3$, $A = 2$, $\tau_1 = 0.5$, e) $\tau_0 \approx 1583.5$, $A = 2$, $\tau_1 = 0.5$, f) $A = 4$, $\tau_1 = 0.5$, g) $A = 3$, $\tau_1 = 0.25$.

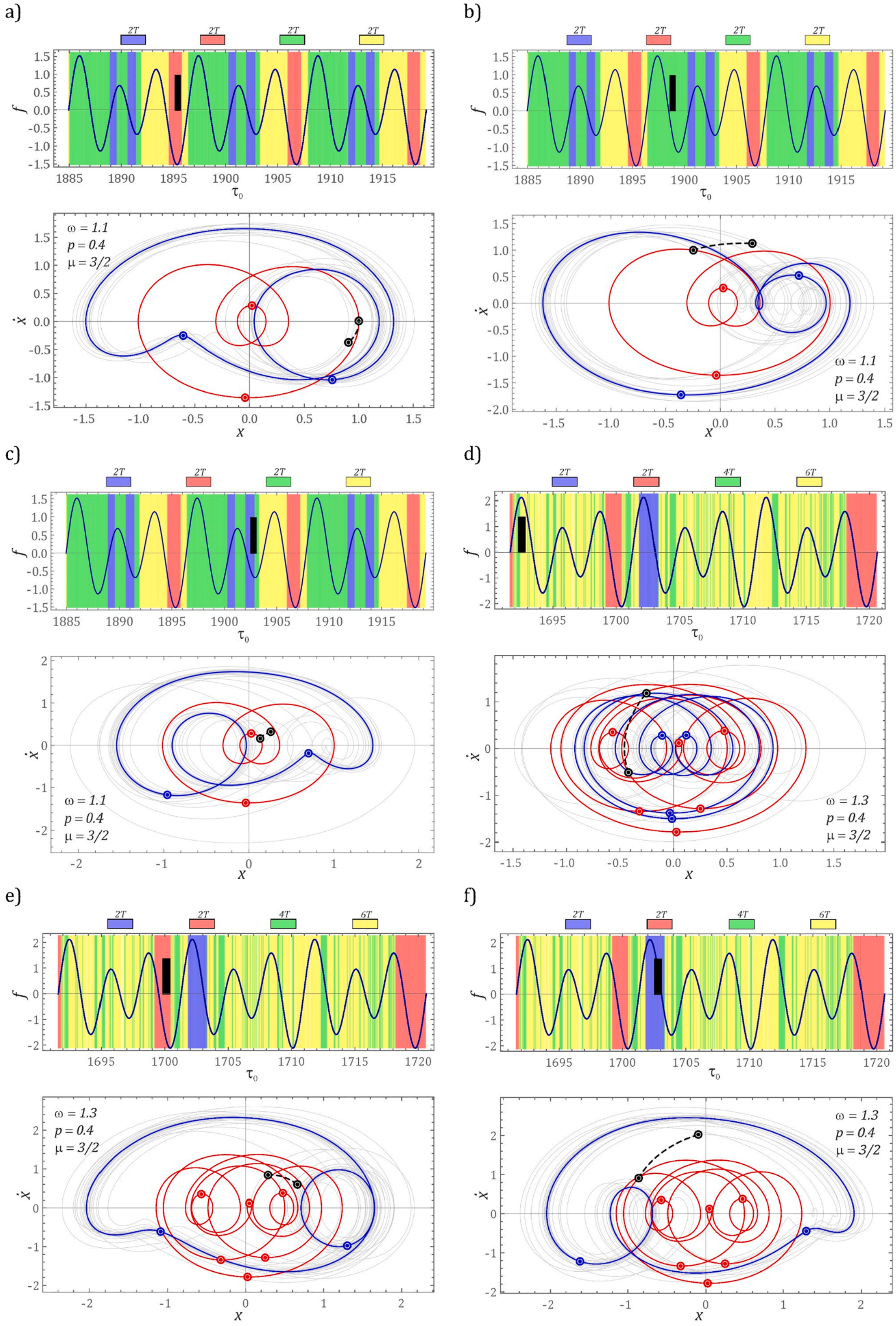

Fig. 12. Model test results: a) $\tau_0 \approx 1895$, $A = 2$, $\tau_1 = 0.5$, b) $\tau_0 \approx 1898.5$, $A = 2$, $\tau_1 = 0.5$, c) $\tau_0 \approx 1902.5$, $A = 2$, $\tau_1 = 0.5$, d) $\tau_0 \approx 1596.5$, $A = 2$, $\tau_1 = 0.5$, e) $\tau_0 \approx 1700$, $A = 2$, $\tau_1 = 0.5$, f) $\tau_0 \approx 1702.5$, $A = 2$, $\tau_1 = 0.5$.

The impulse characteristics were defined by parameters representing the amplitude factor A and the width (activation time) τ_1. If the mechanical vibration signal affecting the energy harvesting system is disturbed by an impulse with the following characteristics: $A = 2$, $\tau_1 = 0.5$, then there is a 76% chance of obtaining a solution with $U_{RMS} > 20$. The diagram (Fig. 9e) illustrates: $A = 6$, $\tau_1 = 0.5$, which results in a 56% chance of obtaining a solution where $U_{RMS} > 20$. The diagram of impulse excitations presented in Fig. 9f was plotted for an impulse of amplitude factor $A = 6$ and width $\tau_1 = 0.25$. In such a case, the probability of moving to an orbit with $U_{RMS} > 20$ is 29.2%.

If the ratio of the frequency of the external source of excitation is based on $\mu = 4/3$ and $\omega = 1.4$, then there are five coexisting periodic solutions, with a periodicity of 3T and 9T. The response of the forced system with zero initial conditions induces a voltage on the piezoelectric electrodes of $U_{RMS} = 9.4$. The maximum possible voltage is $U_{RMS} = 16.5$. This solution is possible if the impulse is initiated in the area mapped with a magenta color (Fig. 10).

The diagram of impulse excitations identified for the assumed impulse profile $A = 2$, $\tau_1 = 0.5$ indicates that the probability of achieving a solution characterized by $U_{RMS} > 15$ is 38.4%. Contrary to the previously considered case, it is possible to use the impulse to correct the response of the system in a wide range of coexisting solutions. Sample images of diagrams of impulse excitations and impulse-corrected phase trajectories are presented in the graphs shown in Fig. 10. It is worth noting that obtaining a 3T-periodic solution, characterized by the voltage $U_{RMS} = 9.1$ (blue basin of attraction in Fig. 7), is difficult due to the very narrow bands corresponding to it, as shown in the diagram.

Fig. 10f shows the structure of the diagram of impulse excitations for: $A = 2$, $\tau_1 = 0.25$, which gives a 14.4% probability of achieving a solution characterized by $U_{RMS} > 15$. The diagram of impulse excitations presented in Fig. 10g was plotted for an impulse with the amplitude factor $A = 2$ and width $\tau_1 = 0.125$. In such a case, the probability of moving to an orbit with $U_{RMS} > 15$ is 0%.

$$\omega_0^2 = \frac{c_B + c_1}{m_{TEH}}, \quad \delta = \frac{b_B}{m_{TEH}\omega_0}, \quad \alpha = \frac{c_2 a_0^2}{c_B + c_1}, \quad \beta = \frac{c_3 a_0^4}{c_B + c_1}, \quad \vartheta = \frac{k_P}{\omega_0^2 a_0 m_{TEH}}, \quad p = \frac{A}{a_0},$$

$$\mu = \frac{\omega_2}{\omega_1}, \quad \omega = \frac{\omega_1}{\omega_0}, \quad x = \frac{y}{a_0}, \quad \vartheta = \frac{k_P a_0}{C_P}, \quad \sigma = \frac{1}{\omega_0 C_P R_Z}, \quad \tau = \omega_0 t.$$

If the frequency ratio of the external source of excitation is based on $\mu = 5/4$ and $\omega = 1.4$, then five coexisting periodic solutions are possible, with a periodicity of 4T and 12T. The system response, with zero initial conditions, induces a voltage on the piezoelectric of $U_{RMS} = 9.4$. In comparison, the probability of obtaining a solution with the highest energy harvesting ability ($U_{RMS} = 20.8$), by initiating with impulse: $A = 2$ and $\tau_1 = 0.5$ is 32.2%. This solution can be obtained if the impulse is initiated in the zone mapped in blue (Fig. 11). Fig. 11f shows the structure of the diagram for impulse excitations characterized by: $A = 4$, $\tau_1 = 0.5$, and that the probability of achieving a solution characterized by $U_{RMS} > 20$ is 7.1%. The diagram of impulse excitations presented in Fig. 11g was plotted for an impulse with the amplitude factor $A = 3$ and width $\tau_1 = 0.5$. For such a case, the probability of moving to an orbit with $U_{RMS} > 20$ is 6.2%.

The diagrams of impulse excitations presented in the graphs (Fig. 9 to Fig. 11), for the most part, are mapped with an irregular arrangement of colors along the axis τ_0, representing the moment of impulse initiation. This issue is out of scope for this paper, however, referring to the relevant images of the diagrams of impulse excitations and the basins of attraction, it is hypothesized that the irregularities of the diagrams may be caused by the fractal structure of the basins. This is justified by the fact that, if the energy harvesting system is influenced by an external excitation, defined by the following parameters: $\omega = 1.1$, $p = 0.4$, $\mu = 3/2$, then the diagram of impulse excitations will assume a fairly regular structure (Fig. 12a-12c). All the coexisting solutions are characterized by the periodicity of 2T, however, only for three of them, the effective value of the voltage induced on the piezoelectric electrodes reaches $U_{RMS} > 10$, which accounts for about 71% of the tested variability range τ_0.

When the value of the dimensionless excitation frequency increases to $\omega = 1.3$, then, for zero initial conditions, the system response is given by a periodic solution with a periodicity of 6T (trajectories plotted in red, Fig. 12d-12f). Similarly to the previous example, four stable periodic solutions are given: two 2T-periodic solutions and one each with 4T and 6T periodicity. The graphic images of the basins of attraction are presented in the preceding section (Fig. 6). Only in relation to 2T-periodic solutions, the voltage $U_{RMS} > 18$ is induced on the piezoelectric electrodes, which represents approximately 18.8% of the tested τ_0 range.

The presented examples demonstrate the influence of the efficiency of energy harvesting by modifying the solution's orbit.

3.4. Comparison of the efficiency of energy harvesting

The numerical tests presented in this subsection are carried out to investigate the comparison of the efficiency of energy harvesting from

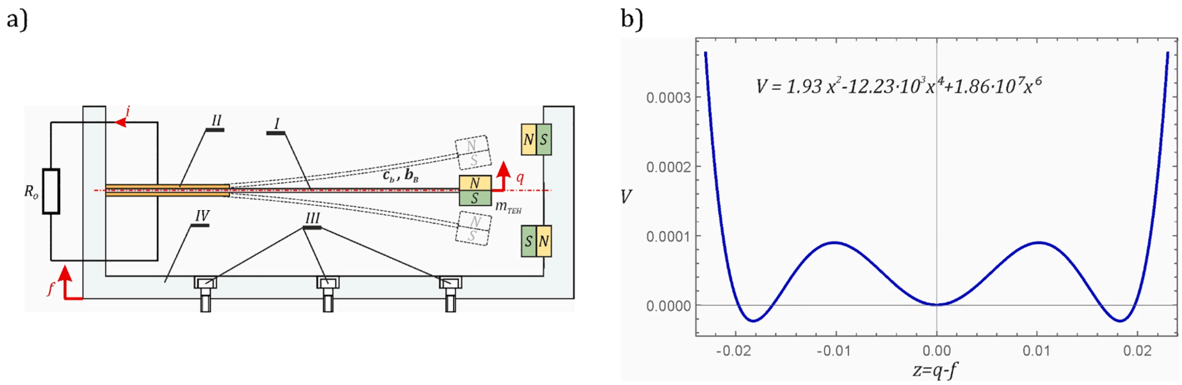

Fig. 13. Tristable energy harvesting system: a) phenomenological model, b) characteristics of the energy potential.

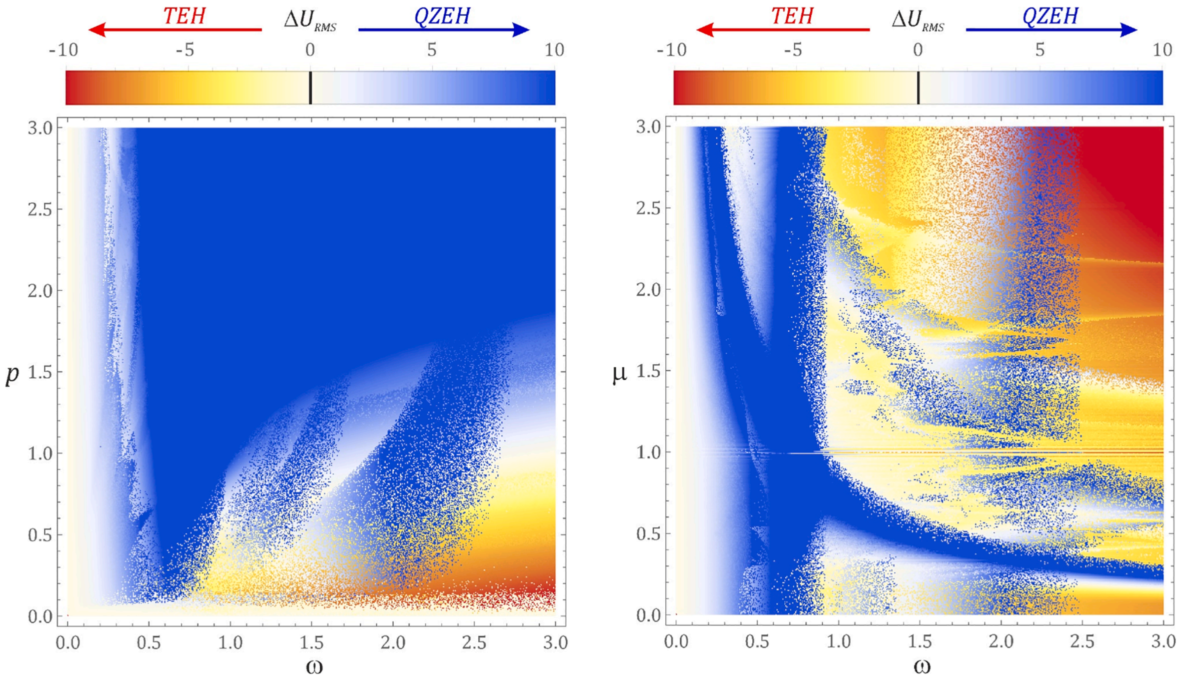

Fig. 14. Multi-colored maps of the energy harvesting effectivity by QZEH and TEH systems, showing the influence of: a) p parameter at $\mu = 0$, b) μ parameter at $p = 0.4$. The maps were drawn assuming random initial conditions.

vibrating machine components by the QZEH system and the tristable TEH system (Fig. 13, eq. (10)).

$$\begin{cases}\ddot{x}+\delta\dot{x}+x+\alpha x^3+\beta x^5+\theta U_P=\omega^2 p\big(sin(\omega\tau)+\mu^2 sin(\mu\omega\tau)\big),\\ \dot{U}_P+\sigma U_P-\vartheta\dot{x}=0.\end{cases} \tag{10}$$

where:

Appropriate model assumptions were made during the computer simulations. One of these concerns the geometric and material dimensions of the flexible beam. Bearing in mind the objective assessment of the efficiency of energy harvesting by individual design solutions, it was assumed that all systems are characterized by the same geometric and material parameters of a flexible beam. Considering the comparable value of the parameter $\omega_0 \approx 30$, it is shown that the m_{TEH} mass loading the flexible beam was properly corrected in the tristable system (TEH). As an indicator of the efficiency of energy harvesting, the difference of the effective values of the voltage induced on the piezoelectric electrodes was adopted: $\Delta U_{RMS} = U_{RMS}^{QZEH} - U_{RMS}^{TEH}$. The results of the numerical tests were visualized in the form of two-dimensional multi-color maps showing the influence of the control parameter p (Fig. 14a) and the frequency ratio μ (Fig. 14b).

The areas highlighted in red represent better efficiency in energy harvesting from vibrating mechanical systems with the tristable potential (TEH) system. Blue indicates more efficient energy harvesting by the system with a quasi-zero potential (QZEH) system. Faded shades of yellow, blue and white on the multi-colored maps indicate comparable

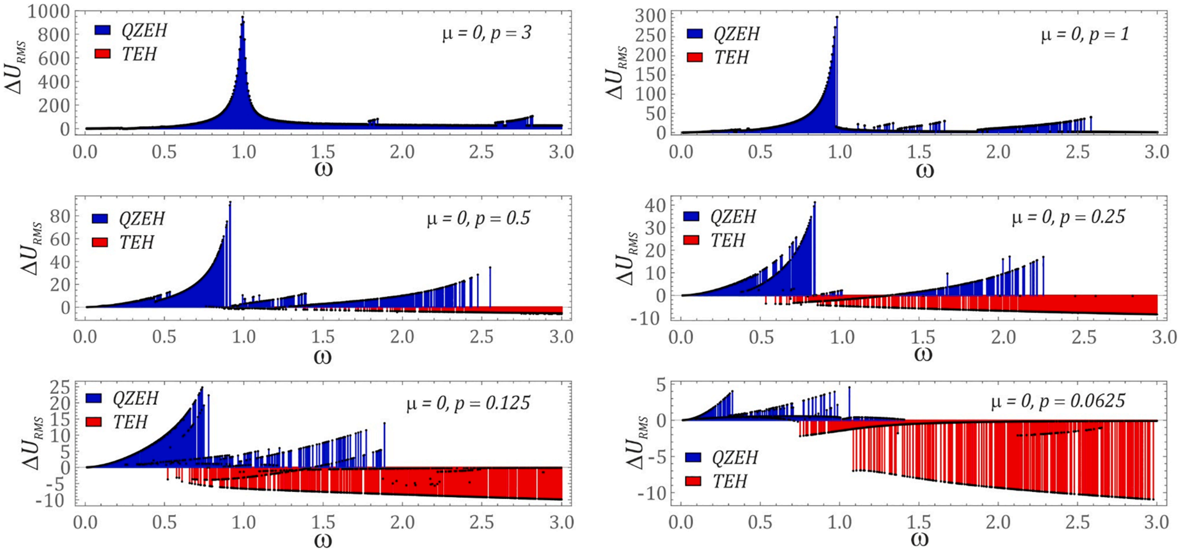

Fig. 15. Diagrams of the difference in RMS voltages induced on piezoelectric electrodes by QZEH and TEH, plotted with the assumption of the variability of the p parameter. The results of the computer simulations were obtained with the assumption of random initial conditions.

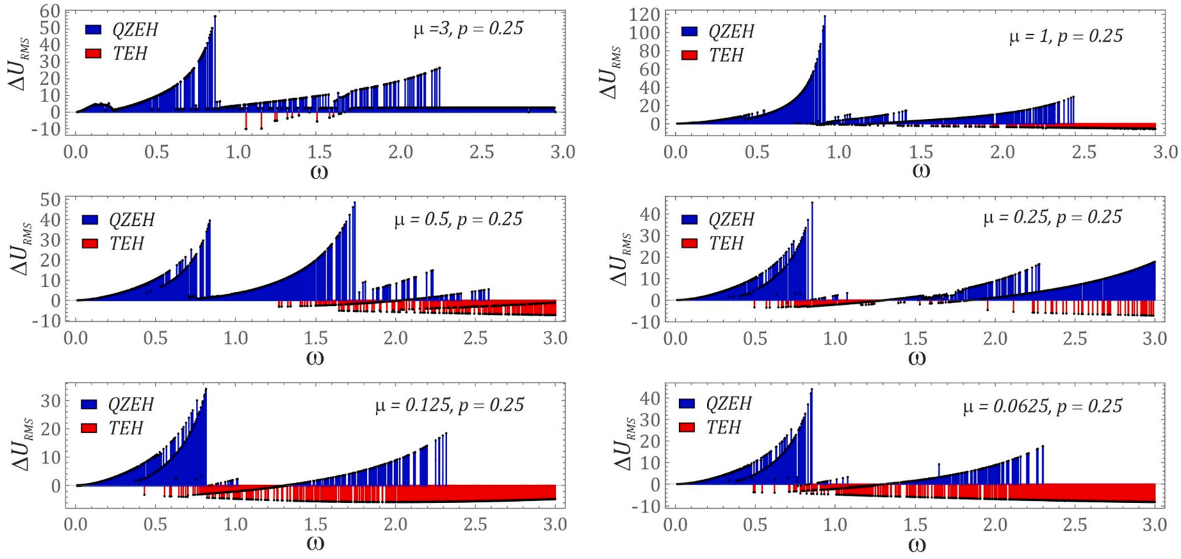

Fig. 16. Diagrams of the difference in RMS voltages induced on piezoelectric electrodes by QZEH and TEH, plotted with the assumption of the variability of the μ parameter. The results of the computer simulations were obtained with the assumption of random initial conditions.

efficiency of energy harvesting by both systems. The multi-colored maps are an important observation when considering the selection of the appropriate design solution for the energy harvesting system.

To illustrate the efficiency of energy harvesting in the considered ranges of variability of control parameters, the legend was arbitrarily limited to the variability range $\Delta U_{RMS} \in [-10, 10]$. This was done because in the range of higher values of the p parameter, the effective values of the voltage induced on the piezoelectric electrodes in the QZEH system reached $U_{RMS} \approx 1000$, in the vicinity of $\omega = 1$ (Fig. 15). Such a large difference makes it difficult to assess the efficiency of energy harvesting by individual design solutions. For this reason, to illustrate the existing differences, sections of multi-colored maps were drawn, corresponding to the selected values of p and μ parameters. Values exceeding $U_{RMS} \approx 200$ may be physically unrealistic because loads acting on a flexible beam have an impact on its fatigue strength and, with prolonged exposure to such force, may lead to its destruction [40].

Diagrams of the difference in values of RMS voltages induced on the electrodes of piezoelectric transducers (Figs. 15, 16), were plotted with twice the resolution of the control parameter ω, in relation to the multi-colored map (Fig. 14a). The obtained results confirm that with the increase of p values, the QZEH system harvests energy more efficiently from mechanical vibrations than the TEH system. In addition, the results suggest that in the low frequency range $\omega < 0.8$, it is advisable to use a system with an almost flat potential well QZEH.

When breaking down a vibration source into a superposition of two harmonic components, it is shown that the QZEH system can be used for a wide range of μ, if the dimensionless frequency $\omega > 0.9$. For higher frequencies $\omega > 2.4$ and $p > 1.5$, it is advisable to use a system with the tristable potential well (Fig. 14b). However, if the dimensionless excitation amplitude $p = 0.25$, then the application of the TEH system is recommended when $\mu < 0.25$ and the dimensionless excitation frequency $\omega \in [0.85, 1.35]$ and $\omega > 2.4$. The diagrams of the difference in the effective value of the induced voltages on piezoelectric electrodes clearly indicate that the design solutions of the quasi-zero potential well system is characterized by a dynamic voltage increase (when the parameters characterizing the excitations p and ω are in the zone of periodic solutions). However, in relation to the tristable system, the voltage increases smoothly on the piezoelectric electrodes, along with the increase in the value of the dimensionless frequency ω.

One should be aware that the results of the presented numerical studies provide important, useful information. However, if using the parameter values $\mu = 0$ and $p = 0.0625$, in the zone $\omega \in [0.5, 1.1]$ (Fig. 15), it is advisable to conduct an additional detailed analysis – this is also true when $\mu = 0.25$ and $p = 0.25$. This is required because random initial conditions are selected once for each value of ω diagrams. Because of this, in relation to the first system, a solution may be characterized by low energy harvesting efficiency. On the other hand, in the case of the latter, the randomly selected initial conditions may lead to a solution with the best energy harvesting efficiency. Therefore, in such situations, it is necessary to carry out a detailed analysis to identify the efficiency of energy harvesting with all coexisting solutions.

4. Conclusions

The results of numerical tests presented in this paper were assessed to study the influence of the parameter μ, defined as the frequency ratio of the two external harmonic forces, on the energy harvesting efficiency of the quasi-zero stiffness system. Moreover, the influence of the μ coefficient on periodicity and the number of coexisting solutions was investigated. Although the effectiveness of energy harvesting systems is currently not very high, they are potentially capable of sufficiently powering some simple measurement systems, such as three-axis accelerometers and wireless data transmission systems. Such systems are useful in the transport industry for monitoring the condition of vehicles. For the comfort of travelers, vehicles that are designed for transporting people are usually designed to minimize the impact of cyclical loads. For this reason, in the presented research, we have limited ourselves to a relatively small amplitude of vibrations. In summary, based on the numerical tests performed, it is possible to draw the following conclusions:

- A correlation was demonstrated between the multi-color map of the distribution of the largest Lyapunov exponent and the diagram of the effective value of the voltage induced on the piezoelectric electrodes.
- The conducted numerical experiments clearly show that to efficiently harvest energy from vibrating mechanical systems, the operating point of the system with quasi-zero stiffness should be located outside of the zones of chaotic solutions.
- The obtained results from numerical tests indicated that when the dimensionless frequency of the excitation ω passes through the “fault”, the number of coexisting solutions is reduced, and thus the efficiency of energy harvesting is reduced.
- The presented numerical tests show that the energy harvesting system with quasi-zero stiffness demonstrates the highest efficiency

when the frequency of mechanical vibrations affecting the system is in the range of $\omega \in [0.6, 1]$ (Fig. 5).

- The information contained in the diagram of impulse excitations (Figs. 9-12) is useful as the basis for the design of an external impulse initiation system that will directly improve the efficiency of an energy harvesting system.
- For most values of the dimensionless excitation amplitude, the QZEH system is more efficient at harvesting energy than the TEH system (Figs. 9–11).
- In the QZEH system, limiting the zones of chaotic solutions is possible by increasing the energy dissipation coefficient b_z.

It is worth emphasizing that the system with quasi-zero stiffness contains elements of the multi-stable system, but instead of the potential barrier, there is a flattening around × = 0, which means that the system can operate effectively, even for small amplitudes of excitations. In such cases, the tristable system is impractical as it cannot jump over the potential barrier between the wells. The published results of computer simulations indicate that the modification of the energy harvesting system design with a passive cyclic pulse excitation subsystem can significantly improve the amount of energy harvested from vibrating mechanical devices.

CRediT authorship contribution statement

Jerzy Margielewicz: Resources, Conceptualization, Methodology, Software, Validation, Formal analysis, Investigation, Data curation, Writing – original draft, Visualization, Supervision, Project administration, Funding acquisition. **Damian Gąska:** Resources, Software, Formal analysis, Investigation, Methodology, Visualization, Writing – original draft, Writing – review & editing. **Grzegorz Litak:** Conceptualization, Methodology, Validation, Writing – review & editing, Funding acquisition. **Piotr Wolszczak:** Conceptualization, Validation, Writing – review & editing, Funding acquisition. **Daniil Yurchenko:** Validation, Writing – review & editing.

Declaration of Competing Interest

The authors declare that they have no known competing financial interests or personal relationships that could have appeared to influence the work reported in this paper.

Acknowledgement

This work was supported by the program of the Ministry of Science and Higher Education in Poland under the project DIALOG 0019/DLG/2019/10 in the years 2019-2021.

References

[1] Chehouri A, Younes R, Ilinca A, Perron J. Review of performance optimization techniques applied to wind turbines. Appl Energy 2015;142:361–88. https://doi.org/10.1016/j.apenergy.2014.12.043.

[2] Xu J, Ni T, Zheng B. Hydropower development trends from a technological paradigm perspective. Energy Convers Manag 2015;90:195–206. https://doi.org/10.1016/j.enconman.2014.11.016.

[3] Zhang Z, Xiang H, Shi Z, Zhan J. Experimental investigation on piezoelectric energy harvesting from vehicle-bridge coupling vibration. Energy Convers Manag 2018;163:169–79. https://doi.org/10.1016/j.enconman.2018.02.054.

[4] Kim P, Son D, Seok J. Triple-well potential with a uniform depth: Advantageous aspects in designing a multi-stable energy harvester. Appl Phys Lett 2016;108(24):243902. https://doi.org/10.1063/1.4954169.

[5] Litak G, Friswell MI, Kitio Kwuimy CA, Adhikari S, Borowiec M. Energy harvesting by two magnetopiezoelastic oscillators with mistuning. Theor Appl Mech Lett 2012;2(4):043009. https://doi.org/10.1063/2.1204309.

[6] Mitcheson PD, Yeatman EM, Rao GK, Holmes AS, Green TC. Energy harvesting from human and machine motion for wireless electronic devices. Proc IEEE 2008;96(9):1457–86. https://doi.org/10.1109/JPROC.2008.927494.

[7] Kim P, Seok J. Dynamic and energetic characteristics of a tri-stable magnetopiezoelastic energy harvester. Mech Mach Theory 2015;94:41–63. https://doi.org/10.1016/j.mechmachtheory.2015.08.002.

[8] Giri AM, Ali SF, Arockiarajan A. Dynamics of symmetric and asymmetric potential well-based piezoelectric harvesters: A comprehensive review. J Intell Mater Syst Struct 2020. https://doi.org/10.1177/1045389X20978292.

[9] Erturk A, Inman DJ. Piezoelectric Energy Harvesting. Chichester, UK: John Wiley and Sons; 2011. https://doi.org/10.1002/9781119991151.

[10] Keshmiri A, Deng X, Wu N. New energy harvester with embedded piezoelectric stacks. Compos Part B Eng 2019;163:303–13. https://doi.org/10.1016/j.compositesb.2018.11.028.

[11] Kundu S, Nemade HB. Modeling and Simulation of a Piezoelectric Vibration Energy Harvester. In: Procedia Eng. Elsevier Ltd; 2016. p. 568–75. https://doi.org/10.1016/j.proeng.2016.05.043.

[12] Lallart M, Zhou S, Yang Z, Yan L, Li K, Chen Yu. Coupling mechanical and electrical nonlinearities: The effect of synchronized discharging on tristable energy harvesters. Appl Energy 2020;266:114516. https://doi.org/10.1016/j.apenergy.2020.114516.

[13] Wang J, Gu S, Zhang C, Hu G, Chen G, Yang K, et al. Hybrid wind energy scavenging by coupling vortex-induced vibrations and galloping. Energy Convers Manag 2020;213:112835. https://doi.org/10.1016/j.enconman.2020.112835.

[14] Daqaq MF, Masana R, Erturk A, Quinn DD. On the role of nonlinearities in vibratory energy harvesting: A critical review and discussion. Appl Mech Rev 2014;66. https://doi.org/10.1115/1.4026278.

[15] Huang D, Zhou S, Litak G. Theoretical analysis of multi-stable energy harvesters with high-order stiffness terms. Commun Nonlinear Sci Numer Simul 2019;69:270–86. https://doi.org/10.1016/j.cnsns.2018.09.025.

[16] Yin Z, Gao S, Jin L, Sun Y, Wu Q, Zhang X, et al. A dual impact driven frequency up-conversion piezoelectric energy harvester for ultralow-frequency and wide-bandwidth operation. Sensors Actuators A Phys 2021;331:112961. https://doi.org/10.1016/j.sna.2021.112961.

[17] Shahruz SM. Design of mechanical band-pass filters with large frequency bands for energy scavenging. Mechatronics 2006;16(9):523–31. https://doi.org/10.1016/j.mechatronics.2006.04.003.

[18] Litak G, Margielewicz J, Gąska D, Wolszczak P, Zhou S. Multiple Solutions of the Tristable Energy Harvester. Energies 2021;14:1284. https://doi.org/10.3390/en14051284.

[19] Zhou S, Cao J, Inman DJ, Lin J, Liu S, Wang Z. Broadband tristable energy harvester: Modeling and experiment verification. Appl Energy 2014;133:33–9. https://doi.org/10.1016/j.apenergy.2014.07.077.

[20] Lai YC, Hsiao YC, Wu HM, Wang ZL. Waterproof Fabric-Based Multifunctional Triboelectric Nanogenerator for Universally Harvesting Energy from Raindrops, Wind, and Human Motions and as Self-Powered Sensors. Adv Sci 2019;6. https://doi.org/10.1002/advs.201801883.

[21] Zou D, Liu G, Rao Z, Zi Y, Liao W-H. Design of a broadband piezoelectric energy harvester with piecewise nonlinearity. Smart Mater Struct 2021;30(8):085040. https://doi.org/10.1088/1361-665X/ac112c.

[22] Granados A. Invariant manifolds and the parameterization method in coupled energy harvesting piezoelectric oscillators. Phys D Nonlinear Phenom 2017;351–352:14–29. https://doi.org/10.1016/j.physd.2017.04.003.

[23] Li X, Zhang J, Li R, Dai Lu, Wang W, Yang K. Dynamic responses of a two-degree-of-freedom bistable electromagnetic energy harvester under filtered band-limited stochastic excitation. J Sound Vib 2021;511:116334. https://doi.org/10.1016/j.jsv.2021.116334.

[24] Kumar R, Gupta S, Ali SF. Energy harvesting from chaos in base excited double pendulum. Mech Syst Signal Process 2019;124:49–64. https://doi.org/10.1016/j.ymssp.2019.01.037.

[25] Jia Y. Review of nonlinear vibration energy harvesting: Duffing, bistability, parametric, stochastic and others. J Intelligent Mater Syst Struct 2020;31:921–44. https://doi.org/10.1177/1045389X20905989.

[26] Margielewicz J, Gąska D, Litak G. Evolution of the geometric structure of strange attractors of a quasi-zero stiffness vibration isolator. Chaos, Solitons and Fractals 2019;118. https://doi.org/10.1016/j.chaos.2018.11.012.

[27] Huguet T, Lallart M, Badel A. Orbit jump in bistable energy harvesters through buckling level modification. Mech Syst Signal Process 2019;128:202–15. https://doi.org/10.1016/j.ymssp.2019.03.051.

[28] Zhang Y, Ding C, Wang J, Cao J. High-energy orbit sliding mode control for nonlinear energy harvesting. Nonlinear Dyn 2021;105:191–211. https://doi.org/10.1007/S11071-021-06616-8.

[29] Fu H, Mei X, Yurchenko D, Zhou S, Theodossiades S, Nakano K, et al. Rotational energy harvesting for self-powered sensing. Joule 2021;5(5):1074–118. https://doi.org/10.1016/j.joule.2021.03.006.

[30] Fei J, Ding H. Adaptive sliding mode control of dynamic system using RBF neural network. Nonlinear Dyn 2012;70(2):1563–73. https://doi.org/10.1007/s11071-012-0556-2.

[31] Prasad LB, Tyagi B, Gupta HO. Optimal Control of Nonlinear Inverted Pendulum System Using PID Controller and LQR: Performance Analysis Without and With Disturbance Input. Int J Autom Comput 2014;11(6):661–70. https://doi.org/10.1007/s11633-014-0818-1.

[32] Lopes VG, Peterson JVLL, Cunha AJ. Nonlinear Characterization of a Bistable Energy Harvester Dynamical System. Springer Proc Phys 2019;228:71–88. https://doi.org/10.1007/978-981-13-9463-8_3.

[33] Roca L de la, Peterson J, Pereira M, Cunha AJ. Control of chaos via OGY method on a bistable energy harvester. 25th ABCM Int. Congr. Mech. Eng. (COBEM 2019), 2019.

[34] Zheng R, Nakano K, Hu H, Su D, Cartmell MP. An application of stochastic resonance for energy harvesting in a bistable vibrating system. J Sound Vib 2014;333(12):2568–87. https://doi.org/10.1016/j.jsv.2014.01.020.

[35] Coccolo M, Litak G, Seoane JM, Sanjuán MAF. Optimizing the Electrical Power in an Energy Harvesting System. Int J Bifurc Chaos 2015;25. https://doi.org/10.1142/S0218127415501710.

[36] Sandri M. Numerical Calculation of Lyapunov Exponents. Math J 1996;6:78–84.

[37] Stefanski A, Dabrowski A, Kapitaniak T. Evaluation of the largest Lyapunov exponent in dynamical systems with time delay. Chaos, Solitons Fractals 2005;23 (5):1651–9. https://doi.org/10.1016/j.chaos.2004.06.051.

[38] Erturk A, Hoffmann J, Inman DJ. A piezomagnetoelastic structure for broadband vibration energy harvesting. Appl Phys Lett 2009;94(25):254102. https://doi.org/10.1063/1.3159815.

[39] De Paula AS, Inman DJ, Savi MA. Energy harvesting in a nonlinear piezomagnetoelastic beam subjected to random excitation. Mech Syst Signal Process 2015;54:405–16. https://doi.org/10.1016/j.ymssp.2014.08.020.

[40] Junak G. Low-cycle fatigue characteristics of selected titanium, magnesium and aluminium alloys. Arch Metall Mater 2018;63:1949–55. https://doi.org/10.24425/amm.2018.125129.